ELEVATION MODELING AND PALAEO-ENVIRONMENTAL INTERPRETATION IN THE SIWA AREA (EGYPT): APPLICATION OF SAR INTERFEROMETRY AND RADARGRAMMETRY TO COSMO-SKYMED IMAGERY

Riccardo Salvini[a*], Luigi Carmignani[a], Mirko Francioni[b], Paolo Casazza[a]

[a] University of Siena, Department of Environment, Earth and Physical Sciences and Centre of Geotechnologies CGT. Via Vetri Vecchi 34, 52027, San Giovanni Valdarno (AR) Italy. Tel. +39 055 9119441, e-mail: riccardo.salvini@unisi.it ([*]corresponding author), luigi.carmignani@unisi.it; paocasazza@gmail.com

[b] Department of Earth Sciences, Simon Fraser University, 8888 University Drive, Burnaby BC Canada, V5A 1S6. Tel. 778-782 6670, e-mail: mfrancio@sfu.ca

ABSTRACT

Digital elevation models produced from COSMO-SkyMed imagery were used to delineate palaeo-drainage in a wide area surrounding the Siwa and Al-Jaghbub oases of the western Sahara Desert (Egypt and Libya). This new generation of synthetic aperture radar imagery is suitable for this purpose because of its high spatial resolution and capacity to penetrate dry surface sediments. Different techniques such as radar interferometry and radargrammetry were used to produce digital elevation models. These were assessed for accuracy and then combined to produce a single elevation model of the area.

The resulting elevation model was used to support the geological study and palaeo-environmental interpretation of the area. It revealed buried features of the landscape, including inactive palaeo-drainage systems. Drainage features were extracted from the elevation model using geographical information systems; results were combined and assessed with respect to geological field data, as well as data from the literature. Previous studies in the area suggest that a wide river, probably the old Nile River, flowed into the Libyan palaeo-Sirte before the Late Messinian drawdown of the Mediterranean Sea. During the Late Messinian lowering of the sea the fluvial system changed shape and carved deep canyons throughout north-eastern Africa.

The reported findings on the key Siwa area were used to precisely delineate the physiography of the modern drainage network and to confirm findings from our previous geological research in the area.

KEYWORDS: Siwa; modern and palaeo-drainage network; COSMO-SkyMed; Interferometry; Radargrammetry

1 – INTRODUCTION

Research, conducted in the framework of the Italian Spatial Agency (ASI) "Announcement of Opportunity" project (Id: 2262), investigated the applicability of high resolution Synthetic Aperture Radar (SAR) imagery for the geological interpretation of drainage systems in an area between the Siwa (Egypt) and Al-Jaghbub (Libya) oases (Fig. 1). The area lies in the Libyan Calansho Desert, between the Qattara Depression and the Egyptian Western Desert, nearly 50 km east of the Libyan border and 560 km from Cairo. About 80 km long and 20 km wide, the study area is located in a deep depression up to -19 m below sea level. Both the Al-Jaghbub area, to the west, and the large Qattara Depression, to the east, lie below sea level.

In this work we investigated the integration of high spatial resolution images, such as those from the COSMO-SkyMed constellation, with the radar beam's ability to penetrate physically homogeneous, fine-grained land surface covers (Schaber et al., 1997). Such remote sensing imagery can provide information on subsurface features not detected by other passive sensors, and are therefore essential for delineating palaeo-morphological settings. In particular, X-band radar waves can theoretically penetrate dry sand to depths of approximately 30 cm without significant attenuation (Schaber et al., 1997). Remotely sensed data is also an important tool for scientists in such poorly accessible areas devoid of roads; moreover, data is easily interpreted due to the lack of vegetation.

This methodology was used to support previous studies on the geology and palaeo-morphology of the area carried out by the Siena University research group (Carmignani et al., 2009). The sand cover in the study area is relatively thin because the area lies on the edge of the Sahara Desert; recent analyses were based on fieldwork, micropaleontological data, and the photointerpretation of passive optical imagery such as Landsat ETM+ and Google Earth™, as well as Digital Elevation Models (DEM) derived from Advanced

Spaceborne Thermal Emission and Reflection Radiometer (ASTER) and Shuttle Radar Topographic Mission (SRTM) data.

Several studies (McCauley et al., 1986; Robinson et al., 2006; Paillou et al., 2009) have made use of radar imagery to investigate palaeo-channels buried under the sand cover. Radar mapping of subsurface features gained wide attention in the early ‘80s thanks to the success of the National Aeronautics and Space Administration's Shuttle Imaging Radar Mission (NASA SIR-A), which revealed channels buried under the sands of the Sahara Desert (McCauley et al., 1982).

Different techniques such as interferometry and radargrammetry were used in this study to create DEMs from COSMO-SkyMed active remote sensing data. Since both methodologies have their peculiarities, advantages and limitations, they were combined in order to obtain a final elevation model with the best possible accuracy compared to GPS data from fieldwork and from a reference DEM. To this end, in the absence of elevation models based on either aerial LIDAR (LIght Detection And Ranging) or aerial photos, a DEM derived from SRTM data was selected as reference. SRTM data have yielded interesting results in previous studies of areas with similar environmental conditions (Ghoneim and El-Baz, 2007; Youssef, 2009). New high spatial resolution DEMs have allowed even more detailed, accurate geomorphological analyses than previous studies; in Carmignani et al. (2009) the study was accomplished by using DEMs with a lower spatial resolution produced from SRTM and ASTER data (the latter from stereophotogrammetry of L1A products).

DEMs generated from COSMO-SkyMed imagery were assessed for accuracy with the goal of checking their reliability and, as a consequence, the correctness of interpretation and accuracy of performed spatial analyses. GIS (Geographic Information System) spatial analysis was then used to automatically extract the drainage network, allowing the identification of recent channels and the interpretative historical reconstruction of possible palaeo-channels and palaeo-environments.

2 - GEOLOGY AND GEOMORPHOLOGY

The geological setting of the area was shaped by tectonic processes and, starting in the Paleozoic, by several transgression-regression cycles. Egypt belongs to the African Craton and is characterized by Paleozoic and more recent basins that were subsequently infilled and modified; the area is extremely stable and not affected by significant endogenous activity. The Miocene rocks, the most frequent in the Western Desert, lie disconformably above the older Precambrian to Oligocene deposits (Tawadros, 2001). National geological maps of Egypt and Libya at a 1:500,000 scale were used along with field data on Libya from the ’70s and ’80s (courtesy of Prof. Luigi Carmignani). The lithologies cropping out in the Siwa area mainly refer to two Miocene formations (Said, 1962; Abdel-Fattah et al., 2013): the *Marmarica* Formation, a fossiliferous shallow-marine carbonate sequence with a few marly intercalations, ascribed to the Middle Miocene, and the continental to shallow-marine clastic sequence of the *Moghra* Formation, dated to the Early Miocene (Fig. 2). The latter formation comprises shale and white sandy carbonate beds, abundant silicified woods, and the uppermost carbonate layers are transitional to the *Marmarica* Formation. East of the study area, the Middle Eocene is represented by the *Mokattam* Group, a transgressive-regressive sequence of neritic limestone with frequent echinoids, *Nummulites gizehensis*, *Nummulites leyelli* and *Nummulites zitteli* and with a white chalky neritic limestone at the base that is underlain by a neritic grey shale. South-east of Siwa, the Late Eocene is represented by the *Qasr el-Sagha* Formation, a littoral marine to continental clastic sequence with oyster beds and coquina layers; intercalations of silt- and claystone are also present. In lower parts, *Nummulites striatus* and *Nummulites fabiani* abound in fossiliferous calcarenite.

This geological setting was confirmed by the micropaleontological analysis of few rock samples collected during fieldwork with the aim of determining the depositional and sedimentary environment in which the lithologies formed. The rock samples were analyzed in collaboration with the Micropaleontology Laboratory of the Earth Sciences Department of *La Sapienza* University in Rome. The collected samples are ascribed to the Middle Miocene due to the presence of the *Neomonoceratinakeiji* species of *Neomonoceratina* (Szczechura and Abd-Elshafy, 1988). The stratotype is the *Marada* Formation, whereas the type locality is located in central Libya, south of the Sirte Basin, between the Marada and Dahra localities (Fig. 1). Analyses confirm the genesis of rocks in the North Western Desert reported in the literature: they belong to the *Moghra* and *Marmarica* formations (Said, 1962), which can be referred respectively to the lower and upper facies of the Middle Miocene *Marada* Formation in Libya (Tawadros, 2001). In the Sirte area, these facies are in turn correlated with the *Rajmah* Formation and the *Al-Jaghbub* Formation (Carmignani et al., 1990). According to Abdel-Fattah et al. (2013) the *Moghra* and *Marmarica* formations can be respectively dated to the Early Miocene (Aquitanian-Burdigalian) and the Middle Miocene (Langhian-Serravallian). None of the Late Miocene and Pliocene sediments crop out in the surroundings of the study area.

The Quaternary cover sediments are represented by *sabkha* (saline, puffy, crusted flat-bottomed basins intersecting the water table and forming a kind of playa) deposits which, near lakes, are intercalated with silt, clay and evaporites. The clastic sedimentary rocks present in the area result from fluvial and gravitational processes within the valleys (locally called *Wadi*). All these sediments lie disconformably above the Middle Miocene *Marmarica* Formation. *Wadi* is an Arabic term traditionally referring to a valley with a dry (ephemeral) riverbed that contains water only during times of heavy rain or simply an intermittent stream. South of the oases, wind erosion produced the currently expanding sand dunes of the Calansho Desert.

The morphology of the area and of the entire Western Desert is the result of long, unceasing peneplanation processes operating since the beginning of the Tertiary. This process has produced a remarkably uniform, generally tabular and desertic landscape with high plateaus in the northern part of the study area and lower ones to the south. The various geomorphic agents have worked together or in turn at different times, producing peculiar morphologies such as the *garats*, small mesas or buttes formed in the Miocene rocks of the area (Fig. 3). Former streams eroded the bedrock, leading to the formation of early *garats*. Wind action and high temperatures subsequently shaped the present mesas and buttes.

Rivers and streams have modelled the landscape, in apparent contrast with the current arid climate conditions and the almost complete absence of active drainage networks. Carmignani et al. (2009) attempted to reconstruct past environmental conditions. They hypothesized that before the Late Messinian drawdown of the Mediterranean Sea (Ryan and Cita, 1978) palaeo-Nile flowed from Asyut (Egypt – Fig. 1), passing south of the Qattara Depression and proceeding in a west-northwest direction through the Siwa and Al-Jaghbub oases, finally reaching the palaeo-gulf of Sirte (Fig. 4). This fluvial system consisted of shallow erosive channels (a few meters at most) in Libya and deeper ones at Siwa (up to some tens of meters). This palaeo-river was characterized by a delta that can still be seen in an area extending more than 100 km along the eastern margin of the palaeo-Sirte, as far as the Calansho Desert boundary (Carmignani et al., 2009).

Geological literature on the Sirte area (Carmignani et al., 1990) describes a second drainage system, represented by the canyons of the Late Messinian drawdown of the Mediterranean Sea, which are clearly visible on optical satellite images. In Libya this palaeo-drainage, which cut and sometimes captured the previous system, is covered by the Pliocene deposits of the *Qarat Weddah* Formation (Di Cesare et al., 1963). Its morphology, characterized by wide, flat-bottomed *wadis* with steep escarpments up to 50-60 m high, is different from that of the pre Late Messinian drawdown of the Mediterranean Sea. The second system can be traced westward from Qarat Weddah to the present Gulf of Sirte and eastward from Siwa to the present Nile Delta. Fig. 4 shows a schematic representation of this reconstruction.

3 – METHODS

The ASI dataset consists of 13 COSMO-SkyMed 2 and 3 tandem Hi-Image STRIPMAP products characterized by 1A SCS-B processing level, Hierarchical Data Format ver. 5 (HDF5) and 3x3 m ground range and azimuth resolution (ASI, 2009). The nominal footprint size is 40 x 40 km, and polarization is horizontal in both transmission and reception (HH). Images were acquired in both ascending and descending orbit configurations with different incidence angles: ranging from 15° to 20° for radargrammetric sets and from 30° to 40° for SAR interferometric sets.

SAR images are stored as Single Look Complex (SLC) files containing both amplitude and phase information on signals backscattered from the ground targets. The dataset was acquired from April to July 2011. The area covered by imagery extends from 24°35’ east - 29°45’ north and 25°35’ east - 29°02’ north. COSMO-

SkyMed (CSKM) images cover this area several times both in ascending and descending orbits: available scenes were therefore divided into two subgroups named “Nile1” and “Nile2” (Fig. 5).

The first area (Nile1), to the east, covers a vast portion the Siwa Oasis comprising the lakes and the numerous *garats* in the surrounding territory. The escarpment of the El-Diffa Plateau characterizes the northern part of the Nile1 area, whereas the dunes of the Calansho Desert characterize the southern landscape. Nile2 comprises the territory northwest of Siwa, including the western portion of the El-Diffa Plateau escarpment, some of the ephemeral lakes east of the Al-Jaghbub Oasis, and the northern dunes of the Calansho Desert. Fig. 6 shows two examples of footprint and quick look of CSKM descending scenes for Nile1 and Nile2 areas.

As mentioned earlier, the study also made use of passive optical images such as Landsat ETM+ (path-row: 176-41, 176-42, 177-41) and Google Earth™, as well as ASTER and SRTM DEMs. The ASTER DEM, called G-DEM, was derived from satellite imagery using photogrammetry; it has a nominal spatial resolution of 30 m. The vertical accuracy of this DEM is about 20 m LE95 (Linear Error at 95% confidence). Data is referred to the Spheroid WGS84 - Datum EGM96 (World Wide 15-minute Geoid Height) and is available in Geotiff format. The SRTM DEM has a nominal spatial resolution of 90 m and its reported vertical accuracy is about 16 m LE90 (at 90% confidence). This DEM has a penetration capability, in dry sand environments, up to depths of 50 cm (Ghoneim and El-Baz, 2007). Data is georeferenced to the WGS84/EGM96 system and is available in Geotiff format. The SRTM DEM and G-DEM were reprojected from the EGM96 Datum to WGS84 for use in interferometric and photogrammetric processing of CSKM images. The accuracy of the reprojected DEMs was subsequently assessed using Ground Control Points (GCP) from the GPS survey completed during fieldwork: differences were always less than 4 m with a standard deviation of 10 m.

The following paragraphs describe the interferometric and radargrammetric processing of SAR data used to produce the DEMs that were subsequently validated and compared to those from the SRTM mission.

3.1 - InSAR PROCESSING

Interferometric SAR (InSAR) processing requires short temporal baselines between images in order to ensure maximum coherence between acquisitions. Coherence may be expressed as a measure of the similarity between the backscattered signal in the area of overlap between two SAR images; it consists of an adimensional number ranging from 0 to 1. Starting from the available set of images and considering different temporal and spatial baselines, two image pairs in right ascending configuration and two in right descending configuration were acquired. Each configuration covers both the Nile1 and Nile2 areas. The temporal offset in a "tandem" configuration, corresponding to a one-day delay between master and slave images, increases the probability of having high coherence between the available data. Fig. 7 shows the InSAR processing workflow.

Before starting interferometric processing, the orbital parameters contained in the scene's metadata were corrected in order to improve the geometric accuracy of the interferometric model and, therefore, the accuracy of the final DEMs. Since ASI did not release precise state vectors of the sensor positions and because metadata contain the most accurate information at the time of delivery, geometric accuracy was improved by using GCPs and modifying the ephemerides of the acquisition time. The coordinates of GCPs were determined during fieldwork and in part derived from Google Earth™ images. Although the overall horizontal accuracy of Google Earth's high resolution imagery varies throughout the world, it is generally greater than 10 m for images acquired prior to year 2008 and better for recent acquisitions (Nagi Zomrawi et al., 2013; Paredes-Hernandez et al., 2013; Ubukawa, 2013; Potere, 2008). Recent high resolution images of the Siwa area refer to the years 2011, 2012 and 2014. A large number of spatially well distributed GCPs were then selected in recent images, and possible outliers were removed. According to the literature (Rodriguez et al., 2006) and to checks made using field-mapped GCPs, height values of GCPs (Z coordinate) were automatically derived from the SRTM DEM.

After correction of the ephemerides, the master and slave images were coregistered. The pairs of granules were coregistered trying to align the SAR scenes precisely so as to accurately determine phase differences, thereby reducing noise. The procedure consists of two steps: the first "coarse coregistration" refers to "pixel-level" accuracy and uses magnitude information to find the offset and shift of the slave image with respect to the master. The second "sub-pixel coregistration" requires the phase information of SLC images.

It is an automatic procedure involving the sub-pixel search for tie points and, after determining the correct transformation equations, slave image resampling. Variable correlation thresholds and grid templates were used and images were subset in order to decrease the computation load by reducing the area to the one investigated. SAR speckle noise was reduced using a Gamma-MAP (or Maximum A Posteriori) filter (Kuan et al., 1987; Lopes et al., 1993). After image coregistration, coherence maps were derived from every interferometric pair. To avoid decorrelation errors that could compromise the calculation of the topographic phase, high coherence values are required to produce interferograms (Ferretti et al., 2007). Decorrelation (especially temporal one) is the main limiting factor for interferometric applications, and it is therefore preferable to use pairs with short temporal baselines (1-2 days maximum) (Zebker and Villasenor, 1992). Interferograms were generated for every SAR image pair with the highest coherence values, so that a total of four interferograms (both ascending and descending orbits) were created for Nile1 and Nile2.

Range variations can be determined by calculating the phase difference between two SAR images. This difference contains the interferometric phase contribution due to terrain morphology, allowing the construction of a DEM. However, the effect of other factors contributing to this difference must be eliminated. For example, phase flattening removes the flat earth contribution, which depends only on the relative position of the two sensors during acquisition. Flattening facilitates interpretation of the topography in the interferogram phase and reduces phase wrapping complexity. Because the residual phase after flattening is directly proportional to terrain height, the residual interferogram looks much like a contour map of terrain height. Furthermore, some filtering operations helped to remove additional phase noises affecting the interferograms. At this point interferograms contain the topography information measured in cycles of $\pm 2\pi$. In this form, the phase is defined as "wrapped". To calculate the correct elevation of each point, the correct integer number of phase cycles must be added to each phase measurement. The "phase unwrapping" method aims to solve the ambiguities of $\pm 2\pi$ intervals. The applied Minimum Cost Flow (MCF) algorithm (Costantini, 1998) for phase unwrapping is particularly effective for errors on the interferogram due to noise and to low coherence especially. The methodology adopted in this study calls for an a-priori DEM (even one with low spatial resolution) that helps to unwrap the phase in areas for which it is extremely difficult or impossible to complete calculations (i.e. oases). The SRTM DEM was selected and projected to the SAR reference system; it was then wrapped in a ±2π interval, thereby forming a simulated interferogram. After the unwrapping process, the calculated height data, still in the SAR reference system (range-azimuth and phase variation coordinates), were geocoded to the cartographic map projection (UTM, WGS84 horizontal and vertical Datum, zone 35 north) using image geometry and orbital parameters. Lastly, residual geometric distortions due to the side-looking geometry of radar images were corrected through filtering and bilinear interpolation resampling. The final grid spacing and Z-factor of DEMs are respectively 10 and 1 m (Fig. 8).

3.2 - RADARGRAMMETRY PROCESSING

Radargrammetry involves the elaboration of SAR image pairs acquired from different incidence angles. It was adopted because it is based on stereoscopy using the intensity component instead of phase (Capalbo et al., 2011). For this reason it has, in principle, the advantage over InSAR of being less affected by atmospheric disturbances (Crosetto and Pérez Aragues, 2000; Méric et al., 2009). This technique can be implemented using various look geometry configurations. The "same-side" configuration, with stereo pairs characterized by the same acquisition mode, was adopted in this study. The pairs were acquired with high intersection angles of approximately 10-20°, and a large area of overlap. High intersection angles correspond to high base/height ratios (B/H), which allow better discrimination of elevation differences among adjacent targets. However, since the backscattering of targets varies according to the beam's angle of incidence, scenes acquired with very different incidence angles are unsuitable for radargrammetry because the backscatter response and geometric distortions (e.g. foreshortening) are totally unrelated. Radargrammetry processing therefore entails a compromise between stereo-viewing and elevation discrimination (Toutin and Gray, 2000).

The processing level, product format and polarization of images were the same as those of InSAR images. Fig. 9 shows the radargrammetry workflow.

There are analogies with the processing of InSAR images; the accuracy of geometric information was improved by modifying the orbital parameters through GCPs. Granules were subset in order to process only the overlapping areas. SAR scenes were also filtered to reduce the speckle noise that would otherwise decrease the effectiveness of image-matching algorithms used to produce geocoded DEMs (Méric et al., 2009). A Gamma-MAP filter was also applied to the images of the Nile1 and Nile2 areas. Coregistration was required to determine the relative orientation of the image pairs with respect to the reference ones. To accomplish this, GCPs from optical satellite images and tie-points were input both manually and automatically. The exact shifts between match and reference images were determined and used to define (through affine transformations based on coefficients calculated from a least-squares optimization) a quasi-epipolar geometry between the images. This geometric configuration is such that only the terrain x-parallax in the flight direction remains. Tie-points also helped to detect the range of parallax in the area between two stereo pairs, which facilitated the size determination of the search window used for automatic matching. This processing was required to produce a precise disparity map containing the parallax values for each resolution cell of the overlap area. A hierarchical strategy based on pyramidal images resampled from the original ones was adopted to reduce mismatch errors and improve processing accuracy (Méric et al., 2009). The x-parallax values of all points in the disparity maps were processed in order to derive the relative elevation values and produce elevation maps in SAR coordinates. As in the case of the InSAR, data relating to image geometry and orbital parameters was used to geocode these maps and create the radargrammetric DEMs. In all, four DEMs with a 10 m spatial resolution were produced for the Nile1 and Nile2 areas, both in ascending and descending orbit configurations (Fig. 10).

3.3 - ACCURACY ASSESSMENT

All the DEMs produced by SAR interferometry and radargrammetry were assessed for accuracy. This allowed the identification of products with better accuracy to be used in the next steps of spatial analysis. This evaluation was used to highlight the pros and cons of the two adopted techniques. The elevation accuracy of DEMs was assessed using the SRTM model as reference due to its largely documented accuracy and because it was produced through interferometric processing of radar images such as the ones under study. Furthermore, the SRTM model was chosen as reference because good results were achieved from the comparison of its elevation data with GCPs from the GPS survey. Several types of analyses were used to define the accuracy of each DEM: statistical, visual, and spatial. Note that possible errors in DEMs generated from SAR data may be ascribed to:

- orbital errors when the exact location of the sensors at the time of acquisition is unknown, leading to inaccuracies in baseline estimation in the case of interferometry and to uncertainties in geometric reconstructions in the case of radargrammetry;
- errors due to a large baseline, unsuitable for interferometric pairs, which affects the coherence between images;
- errors caused by atmospheric disturbance, which affects the quality of interferometric DEMs especially;
- errors due to speckle noise, which affects the accuracy of image matching in radargrammetry;
- errors due to different incidence angles, resulting in different backscattering values from the same area in different acquisitions;
- errors in coregistration and image processing.

Errors can be divided into three categories:

- systematic errors, due to procedures and systems used in the generation of the DEMs;
- random errors, due to unknown and accidental causes or inaccuracies during processing;
- gross errors (blunders), of larger scale and magnitude, easily identified through visual inspection.

Landscape features are represented with a high level of detail in DEMs produced by SAR interferometry. These DEMs clearly highlight incisions due to local drainage and structures sculpted by modelling agents. Despite this high level of detail, some areas lack data (void pixels) or contain errors.

Although DEMs produced by radargrammetry are much less dense than those produced by interferometry, they are not affected by the systematic errors generally located in wide morphological depressions and oasis water bodies. Overall, radargrammetric DEMs can be used to discern certain morphological details that are invisible on medium-low resolution SRTM and ASTER DEMs.

The accuracy of models, as already said, was determined and statistically analyzed with respect to the SRTM reference DEM. The value of residuals, expressed as the difference in elevation between the SRTM DEM and the one being assessed, was derived through GIS Map Algebra analysis. The accuracy of DEMS is expressed by the mean value, the standard deviation and the Root Mean Square Error (RMSE). Tab.1 shows the statistical parameters calculated for all the DEMs. It proves that, especially for Nile2, all the models have low RMSE values and standard deviations that are less than or nearly equal to the accuracy of the SRTM DEM. Only the DEM of Nile1, provided by SAR interferometry of ascending granules, shows very large statistical errors with respect to the reference DEM. The different attempts to process the image pairs were unsuccessful, and it was impossible to compensate decorrelation (note that we only have an image pair to be processed, so any important decorrelation cannot be solved). Errors in the DEM were easily spotted by visual inspection.

In general, the interferometric products of the Nile1 group yielded the worst results, whereas the radargrammetric DEMs of this group yielded better statistical results. DEMs (both interferometric and radargrammetric) of the Nile2 area have high statistical accuracy. DEMs from radargrammetry data seem to be the most accurate in this area. These results suggest that the combined use of the two techniques may yield better results. Map Algebra operations in a GIS environment allowed the spatialization of the calculated accuracy such that residuals and their magnitude were easily determined and located (Fig. 11).

Tab.2 shows the classification of elevation residuals and their relative percentages.

The spatial analysis of the main differences, characterized by residuals of higher magnitude, reveals how "errors" are mainly located in well defined areas; in the interferometric DEMs, these areas coincide with water bodies, where spatial decorrelation significantly affects elevation model construction. In particular, high residuals are found in the two Siwa and Al-Jaghbub oases and in the small surrounding lakes and vegetated areas.

InSAR in the Nile1 area yielded the worst results; this may be linked to the low coherence between granules and possible mistakes in the reconstruction of the spatial baseline due to inaccuracies in orbital parameters. It may also be affected by temporal decorrelation due to atmospheric interference although the tandem CSKM images of the area refer to May 24 and 25, 2011, when visibility was about 10 km, there were no precipitation, and the average humidity was around 20% (Weather Underground Inc., 2014). Nevertheless, atmospheric interference can influence the phase value of the backscatter signal to the sensor, compromising the quality of the DEM derived from interferometry data (Crosetto and Pérez Aragues, 2000).

The good accuracy of DEMs of both areas (Nile1 and Nile2) produced by radargrammetry can be explained, as mentioned earlier, by the lower influence of atmospheric conditions on this technique. However, some residuals are high in areas where the automatic image-matching algorithms failed and, consequently, the morphology was misrepresented. For example, the area covered by the dunes of the Calansho Desert, where both the homogeneity of radiometric backscatter and the risk that the same target changes its radiometric value in different scenes because of the wind, make matching difficult and cause errors in the automatic process.

The intrinsic accuracy of the produced DEMs was assessed by comparing them to each other without considering the reference SRTM DEM. Elevation models derived from data with different acquisition geometries (ascending and descending orbits) and using different techniques (InSAR and radargrammetry) were intersected and the resulting differences in elevation analyzed. This study was done to assess the weight of intrinsic errors caused either by the characteristics of the original image datasets (i.e. baselines, temporal and spatial correlation, acquisition geometry) or by user processing. The residuals of these comparisons are reported in Tab.3, which shows their mean value, standard deviation and RMSE for the Nile2 area. The resulting values are very stable, suggesting that the created models are not affected by errors in processing. Since the DEMs were produced using different input data and processing methods, systematic errors in procedures would affect the different models in different ways and to a different extent. In Tab.3 note that the altitude values in ascending orbit DEMs are always higher (and more accurate, see Tab.1) than those in descending orbit DEMs. This fact may be linked not only to the different geometric characteristics of the baseline, but also to the relationship between the acquisition mode (right-looking in both ascending and descending orbits) and the morphology of the area. DEMs produced from ascending scenes probably provide a more accurate representation of the northwest-southeast trending *garats*, which are orthogonal to the sensor view direction (about 83° N).

Considering the vertical accuracy of the reference DEM (±16m LE90), the models produced in this work, thanks to the advanced technology of the COSMO-SkyMed constellation, could be considered very accurate, and the calculated elevation differences could be ascribed to erroneous values of the SRTM DEM; further studies and differential GPS measurements are required to clarify this aspect.

3.4 - DATA FUSION

In order to create a final single DEM of the area with maximum accuracy and reliability, the models from the two areas derived from different techniques were merged using an *ad hoc* GIS procedure. The areas affected by high errors or artefacts were discarded, as well as the pixels or groups of pixels with no elevation values (voids). Data fusion was based on the RMSE derived during accuracy assessment. The eight DEMs were combined and the most accurate values were selected after comparison with the SRTM DEM. Selected values with the lowest residuals were chosen to represent the final elevation of the area, whereas differences greater than or smaller than 10 m were set to “null”. The pixels with the greatest vertical accuracy were then mosaiced, and the remaining “null” values were replaced by elevation data from the SRTM DEM appropriately resampled to a 10 m spatial resolution. Lastly, void-filling operations (Reuter et al., 2007) were applied to the mosaic in order to refine the shape of the surface and enhance smoothness and continuity (Fig. 12).

3.5 - DRAINAGE EXTRACTION

The final DEM was used in the morphometric analysis of the area, which aimed to outline the present drainage pattern and possible buried palaeo-channels. The system's resolution and the radar beam's capacity to penetrate thin sand covers are such that it is technically possible to delineate buried hydrographic systems and investigate the palaeo-morphology of arid desert environments (Ghoneim and El-Baz, 2007; Farr et al., 2007).

The hydrographic pattern was extracted through an automated procedure based on GIS spatial analysis. The adopted D8 flow direction algorithm (Jenson and Domingue, 1988) is well-suited for the identification of individual channels, channel networks and basin boundaries. The algorithm assigns to each cell of the DEM a value representing the direction to the adjacent cell with the steepest downward slope. The flow of water is traced downhill from all points of the DEM, and the cell value is incremented in a new grid for all the downstream points. Lastly, the drainage network is defined by the relative counts of the cells that have a value greater than a certain threshold. In this paper, following the suggestions of Maidment (2002) for the correct determination of a flow, a threshold of 1% of the maximum cumulative flow was chosen. This threshold increases the area required to generate a channel and therefore less areas will respond the requirements. In this way the number of visible channels decreases, primarily for the benefit of the larger channels and dominant in a basin. Fig. 13 shows the drainage network automatically extracted from the final DEM using this procedure.

The resulting drainage lines were assessed by photointerpretation and compared with drainage lines automatically extracted from the SRTM and ASTER DEMs in order to define the final patterns and establish their origin and age as accurately as possible.

4 - DISCUSSION

The final DEM produced from COSMO-SkyMed STRIPMAP images revealed various drainage networks and systems with diverse shapes and characteristics. Results confirm the presence of palaeo-channels in an area extending for more than 4,000 km^2 from the Siwa Oasis, in the east, to the Al-Jaghbub Oasis in the west. The northern area comprises part of the El Diffa Plateau, the southern area negative landforms of the two oases separated by *garats* and sand dunes of the Calansho Desert. Visual inspection of the DEM and satellite imagery clearly reveals an earlier northwest-southeast trending drainage system, nowadays testified by the presence of aligned *garats* (Fig. 14). In our interpretation, this hydrographic system is related to a big palaeo-drainage involving a large part of the Western Desert. This system is similar to the one west of the study area (in and west of the Qarat Weddah area) described in Carmignani et al. (2009). This drainage cut the Middle and Early Miocene *Marmarica* and *Moghra* carbonate platform formations. Based on the characteristics of the *Sahabi* Formation (Carmignani et al., 1990) in the Gulf of Sirte, Carmignani et al. (2009) referred this earlier system to the Tortonian-Early Messinian (Fig. 4). Fig. 15 shows the hypothesized pattern of the drainage network during the Late Messinian salinity crisis from Asyut (Egypt) up to the Gulf of Sirte.

The automatic drainage lines extracted from the CSKM DEM (Fig. 13) do not include the earlier northwest-southeast bedrock incision pattern because of the chosen flow accumulation threshold and the actual topography. On the contrary, they delineated a different system consisting of two networks with different shapes, catchment areas and flow directions. The first, located in the Nile2 area, comprises the Al-Jaghbub Oasis and flows to the W-NW, joining the westernmost systems of Carmignani et al. (2009); the second, in the surroundings of Siwa (Nile1 area) flows to the E-SE, joining the easternmost systems photointerpreted by the same authors south of the Qattara Depression (Fig. 4). The morphology of these networks is markedly different from the erosional system pre Mediterranean Sea drawdown. The watershed separating the two drainage lines extracted from the CSKM DEM is clearly identified west of Siwa Oasis (Fig. 13). This feature, which was practically imperceptible in the field and in earlier remotely sensed data, represents the geographical divide between the two drainage systems in the area. The automatically extracted drainage lines are probably related to the peculiar setting of north Africa in the Late Messinian. During this period, the important marine regression that affected the Mediterranean Sea changed the entire physiography of the area and, consequently, its regional hydrography (Ryan and Cita, 1978). Due to the change in topographic gradient, headward erosion cut new channels in the bedrock that were later partially buried by Pliocene and Quaternary deposits (Said, 1962). At this stage, two drainage networks developed in opposite directions (Fig. 16). One system flowed westward and is still visible in Libya from the area north of Qarat Weddah up to the old Sahabi lagoon (Fig. 15); the palaeo-channels clearly cut the drainage pre Mediterranean Sea salinity crisis. *Wadi al Hamim* and *Wadi al Maqar*, described in Carmignani (1984), Giglia (1984), and Giammarino (1984), are two examples of channels carved in the Middle Miocene Cyrenaica carbonate platform. In the Sirte area these palaeo-channels flowed into the Sahabi channel (Barr and Walker, 1973), a canyon with a depth of about 400 m and a width of 5 km carved in the carbonate platform. Griffin (2011) uses the name Eosahabi for this channel of Messinian age and older, while the term Sahabi is used by the author for a river system of Pliocene age and younger.

At the same time headward erosion reached the Al-Jaghbub Oasis, where, thanks to the network automatically extracted from CSKM data, the uppermost section of the Libyan Late Messinian drainage can be identified. Drainage around the Al Jaghbub Oasis, which roughly corresponds to the Nile2 area, is therefore probably associated with this system.

A second system flowed eastward, forming deep canyons that are in part still visible along the course of the present Nile River (i.e. Asyut, Aswan in Egypt – Fig. 1). In our hypothesis, this system captured first the Miocene palaeo-Nile south of the Qattara Depression and then its upstream portion near Asyut, totally cutting off the previous drainage and forming the present course of the Nile River. In this system, surface waters of the North Western Desert were conveyed to the sea in deep canyons (at the time the base-level was significantly lower than the present one); north of Cairo, these incisions reached a depth greater than 2,500 m (Choumakov, 1967; Said, 1990) and are now filled by Plio-Quaternary sediments. The drainage automatically extracted from the CSKM DEM of the Nile1 area, in the surroundings of Siwa, must be related to this Late Messinian system. Because the pattern and direction of this drainage is similar to that photointerpreted in the Qattara Depression, it may represent either the Late Messinian palaeo-Nile or one of its left-bank tributaries. We therefore suggest that they belonged to the same drainage system, although additional information is required, particularly for the area between Nile1 and Qattara Depression.

During the Pliocene a marine transgression occurred throughout the Mediterranean area (Ryan and Cita, 1978); the deposits (e.g. *Qarat Weddah* Formation in Libya) completely covered the Miocene carbonate platform and its drainage systems (both the Late Messinian canyons and the remains of the previous system – Fig. 17). At that age, the channel Sahabi was not as deep as the Nile canyons because probably already deactivated by a river capture that occurred to the south (this would also explain the different thickness of the Pliocene deposits that are found at the same latitudes in the two palaeo-valleys).

South of Qarat Weddah, a river system characterized by a large fan that covered the southernmost portions of the pre-Messinian drainage (the Sarir Dalmah alluvial fan of Pachur and Altmann, 2006) transported the sands produced by the erosion of the Nubian sandstones (cropping out extensively in southern Libya). These sands formed the Pliocene sediments that lie disconformably above the Miocene carbonate platform and buried its surface drainage channels.

At the same time, in Egypt, the Pliocene transgression affected the Late Messinian canyons of the Nile River; the rise in sea level formed a narrow gulf reaching up to Aswan (Said, 1990), flooding completely the current delta. The deposits of this period are well documented and contain rich marine faunas (Said, 1990).

Later, during the Quaternary, a new regression reactivated the Late Messinian drainage system (Fig. 18). The Quaternary regression, dated to the Tyrrhenian (Late Pleistocene) was less incisive than the Late Messinian one, and the original canyons maintained the thick Pliocene deposits that the new rivers failed to completely erode (Carmignani et al., 1990). Nevertheless, the climate became very arid and, starting in the Early Pleistocene, wide areas of northeast Africa became desertic. The trade winds partially eroded the Pliocene sediments lying above the palaeo-drainage (Brookes, 2001) and deposited them to the south, forming the sand sheet deposits and dunes of the Calansho Desert, even reaching the Tibesti Plateau about 1,000 km south of the Gulf of Sirte. Wind bared the northern areas especially, revealing structures pertaining to the earlier drainage systems, modelling the present-day *garats,* and uncovering traces of ancient, fossil river beds. According to Di Cesare et al. (1963), during the Quaternary pluvial stages (i.e. Saharan I and II of Mousterian - Said, 1990), drainage was from south to north and was partially superimposed on the Late Messinian network.

The proposed chronological evolution of the Siwa area is also supported by the presence of well-preserved morphological features such as the *garats*, typical of this area. These were formed by the erosive action of a big river acting before the Late Messinian. During the Late Messinian this area was not deeply eroded due to its proximity to the watershed that preserved the older morphological landscape. There was probably no intense erosion of the Siwa area in the following epochs.

CONCLUSIONS

SAR interferometry and radargrammetry applied to high spatial resolution images from the COSMO-SkyMed constellation were successfully used to create the digital elevation model and trace the drainage network in the Siwa area. The catchment areas of two networks were delimited and the watershed between the "Libyan" system, flowing westward to the Sirte area, and the "Egyptian" one, flowing eastward, was identified.

Recent attempts to identify and extract the detected hydrography from other DEMs such as SRTM and ASTER were unsuccessful. The photointerpretation of high-resolution passive optical imagery did not reveal such morphological detail. Moreover, thanks to the penetrative capabilities of the radar beam, the southern part of automatically extracted drainage lines shows a prevailing northward direction of flow. These drainage networks (located in the area covered by the Calansho and Western deserts sand sheet - Figs. 13 and 18) could be linked to the Quaternary regression phase during which the ancient drainage was reactivated, as documented by Di Cesare et al. (1963).

The reported results provide additional important data and evidence in support of the hypothesis proposed by Carmignani et al. (2009). Results also provide new starting points for future detailed geological and palaeo-environmental studies of the area. The idea that there was a palaeo-Nile flowing from Egypt to the Gulf of Sirte, in Libya, is very striking but needs to be confirmed by additional data. Further research, including fieldwork, geophysical investigation and processing of additional high-resolution radar data, in the area between the Nile1 and Qattara Depression areas may clarify the physiography of these drainage systems and, in general, the global palaeo-hydrographic setting of north-eastern Africa. This paper confirms how remotely sensed data can be a fundamental tool and source of information for the analysis of vast and remote areas.

ACKNOWLEDGMENTS

We gratefully acknowledge Ruggero Matteucci and Johannes Pignatti (*La Sapienza*, University of Rome), Francesco Checchi (ENI S.p.A., IOEC), Filippo Bonciani and Debora Graziosi (University of Siena) for their collaboration. Research was supported by the ASI in the framework of the COSMO-SkyMed Announcement of Opportunity project "Application of COSMO-SkyMed data for geological researches in Egypt and Libya".

REFERENCES

Abdel-Fattah, Z.A., Kora, M.A., & Ayyad, S.N. (2013). Facies architecture and depositional development of Middle Miocene carbonate strata at Siwa Oasis, Northwestern Egypt. Facies, 59(3), 505-528, http://dx.doi.org/10.1007/s10347-012-0332-2.

ASI (2009). COSMO-SkyMed SAR Products Handbook.

Barr, F.T., & Walker, B.R. (1973). Late Tertiary channel system in northern Libya and its implications on Mediterranean sea level changes. Initial Reports of the Deep Sea Drilling Project, 13, 1244-1250.

Brookes, I.A. (2001). Aeolian erosional lineations in the Libyan desert, Dakhla region, Egypt. Geomorphology, 39(3), 189-209, http://dx.doi.org/10.1016/S0169-555X(01)00026-5.

Capaldo, P., Crespi, M., Fratarcangeli, F., Nascetti, A., & Pieralice, F. (2011). DSM generation from high resolution COSMO-SkyMed imagery with radargrammetric model . In: ISPRS Hannover WorkShop 2011 high-resolution Earth Imaging for Geospatial Information. The International Archives of the Photogrammetry, Remote Sensing and Spatial Information Sciences, Vol. XXXVIII-4/W19, Heipke, C.; Jacobsen, K.; Rottensteiner, F.; Müller, S.; Sörgel, U., ISSN: 1682-1777, Hannover (Germany), June 14-17, 2011.

Carmignani, L. (1984). Geological Map of Libya, Explanatory Booklet, Sheet: Wadi al Hamim, NH 34-7. Tripoli (Libya): Industrial Research Centre.

Carmignani, L., Giammarino, S., Giglia, G., & Pertusati, P. (1990). The Qasr as Sahabi succession and the Neogene evolution of the Sirte Basin (Libya). Journal of African Earth Sciences, 10(4), 753-769, http://dx.doi.org/10.1016/0899-5362(90)90042-D.

Carmignani, L., Salvini, R., & Bonciani, F. (2009). Did the Nile River flow to the Gulf of Sirte during the late Miocene? Italian Journal of Geosciences, 128(2), 403-408, http://dx.doi.org/10.3301/IJG.2009.128.2.403.

Choumakov, I. S. (1967). Pliocene and Pleistocene deposits of the Nile Valley in Nubia and Upper Egypt. Academy of Science of the USSR, transaction of the Geological Institute, 170, 1-110.

Costantini, M. (1998). A novel phase unwrapping method based on network programming. IEEE Transactions on Geoscience and Remote Sensing, 36(3), 813-821, http://dx.doi.org/10.1109/36.673674.

Crosetto, M., & Pérez Aragues, F. (2000). Radargrammetry and SAR Interferometry for DEM Generation: Validation and Data Fusion. Proceedings of CEOS SAR workshop, ESA SP-450, 367-373.

Di Cesare, F., Franchino, A., & Sommaruga, C. (1963). The Pliocene-Quaternary of Giarabub Erg Region. Proceedings of First Sharan Symposium. Revue de l'Institut Francais Du Petrole, 18, 10-11.

Farr, T., Rosen, P., Caro, E., Crippen, R., Duren, R., Hensley, S., Kobrick, M., Paller, M., Rodriguez, E., Roth, L., Seal, D., Shaffer, S., Shimada, J., Umland, J., Werner, M., Oskin, M., Burbank, D., & Alsdorf, D. (2007). The Shuttle Radar Topography Mission. Reviews of Geophysics, 45(2), 2-43, http://dx.doi.org/10.1029/2005RG000183.

Ferretti, A., Monti-Guarnieri, A., Prati, C., Rocca, F., & Massonnet, D. (2007). Part A: Interferometric SAR image processing and interpretation. In: Fletcher, K. (eds) InSAR Principles: Guidelines for SAR Interferometry Processing and Interpretation. Noordwijk (The Netherlands): ESA Publications Division (http://www.esa.int/esapub/tm/tm19/TM-19_ptA.pdf).

Ghoneim, E., & El-Baz, F. (2007). The application of radar topographic data to mapping of a mega-paleodrainage in the Eastern Sahara. Journal of Arid Environments, 69(4), 658-675, http://dx.doi.org/10.1016/j.jaridenv.2006.11.018.

Giammarino, S. (1984). Geological Map of Libya, Explanatory Booklet, Sheet: Wadi al Khali, NH 34-8. Tripoli (Libya): Industrial Research Centre.

Giglia, G. (1984). Geological Map of Libya, Explanatory Booklet, Sheet: Ajdabiya, NH 34-6. Tripoli (Libya): Industrial Research Centre.

Griffin, D.L. (2011). The late Neogene Sahabi rivers of the Sahara and the hamadas of the eastern Libya–Chad border area. Palaeogeography, Palaeoclimatology, Palaeoecology, 309(3–4), 176-185, http://dx.doi.org/10.1016/j.palaeo.2011.05.007.

Jenson, S.K., & Domingue, J.O. (1988). Extracting topographic structure from digital elevation data for geographic information system analysis. Photogrammetric engineering and remote sensing, 54(11), 1593-1600.

Klitzsch, E., List, F., & Pohlmann, G. (1987). Geological map of Egypt (1:500,000 - 24 sheets). Cairo (Egypt): Conoco Coral and Egyptian General Petroleum Corporation.

Kuan, D.T., Sawchuk, A.A., Strand, T.C., & Chavel, P. (1987). Adaptive Restoration of Images with Speckle. IEEE Transactions on Acoustics, Speech, and Signal Processing, 35(3), 373-383, http://dx.doi.org/10.1109/TASSP.1987.1165131.

Lopes, A., Nezry, E., Touzi, R., & Laur, H. (1993). Structure detection and statistical adaptive speckle filtering in SAR images. International Journal of Remote Sensing, 14(9), 1735-1758, http://dx.doi.org/10.1080/01431169308953999.

Maidment D.R. (2002). Arc Hydro: GIS for water resources, vol. 220. ESRI press, Redlands, 203 pp.

McCauley, J.F., Breed, C.S., Schaber, G.G., Mchugh, W.P., Issawi, B., Haynes, C.V., Grolier, M.J., & Kilani, A.E. (1986). Paleodrainages of the Eastern Sahara-The Radar Rivers Revisited. IEEE Transactions on Geoscience and Remote Sensing, GE-24(4), 624-648, http://dx.doi.org/10.1109/TGRS.1986.289678.

McCauley, J.F., Schaber, G.G., Breed, C.S., Grolier, M.J., Haynes, C.V, Issawi, B., Elachi, E., & Blom, R. (1982). Subsurface valleys and geoarcheology of the eastern Sahara revealed by Shuttle radar. Science, 218(4576), 1004-1020, http://dx.doi.org/10.1126/science.218.4576.1004.

Méric, S., Fayard, F., & Pottier, E. (2009). Radargrammetric SAR image processing. Geoscience and Remote Sensing. In: Pei-Gee Peter Ho (Eds.), Geoscience and Remote Sensing, Intech pp. 421–454, http://dx.doi.org/10.5772/8300.

Nagi Zomrawi, M., Ahmed, G. & Hussam Eldin, M. (2013). Positional Accuracy Testing of Google Earth. International Journal of Multidisciplinary Sciences and Engineering, 4(6), 6-9.

Pachur, H.J., Altmann, N. (2006). Die Ostsahara im Spätquartär: Ökosystemwandel im größten hyperariden Raum der Erde. Springer, Berlin.

Paillou, P., Schuster, M., Tooth, S., Farr, T., Rosenqvist, A., Lopez, S., & Malezieux, J.M. (2009). Mapping of a major paleodrainage system in eastern Libya using orbital imaging radar: The Kufrah River. Earth and Planetary Science Letters, 277 (3-4), 327-333, http://dx.doi.org/10.1016/j.epsl.2008.10.029.

Paredes-Hernandez, C.U., Salinas-Castillo, W.E., Guevara-Cortina, F., & Martinez-Becerra, X. (2013). Horizontal positional accuracy of Google Earth's imagery over rural areas: a study case in Tamaulipas, Mexico. Boletim de Ciências Geodésicas, 19(4), 588-601.

Potere, D. (2008). Horizontal positional accuracy of Google Earth's high-resolution imagery Archive. Sensors, 8 (12), 7973-7981, http://dx.doi.org/10.3390/s8127973.

Reuter, H.I., Nelson, A., & Jarvis, A. (2007). An evaluation of void-filling interpolation methods for SRTM data. International Journal of Geographical Information Science, 21(9), 983-1008, http://dx.doi.org/10.1080/13658810601169899.

Robinson, C.A., El-Baz, F., Al-Saud, T.S.M., & Jeon, S.B. (2006). Use of radar data to delineate palaeodrainage leading to the Kufra Oasis in the Eastern Sahara. Journal of African Earth Sciences, 44(2), 229-240, http://dx.doi.org/10.1016/j.jafrearsci.2005.10.012.

Rodriguez, E., Morris, C.S., & Belz, J.E. (2006). A Global Assessment of the SRTM Performance. Photogrammetric Engineering and Remote Sensing, 72(3), 249-260.

Ryan, W.B.F., & Cita, M.B. (1978). The nature and distribution of Messinian erosional surfaces. Indicators of a several-kilometer-deep Mediterranean in the Miocene. Marine Geology, 27(3-4), 193-230, http://dx.doi.org/10.1016/0025-3227(78)90032-4.

Said, R. (1962). The Geology of Egypt. New York (United States): Elsevier, 377 pp..

Said, R. (1990). The Geology of Egypt. Taylor & Francis Group.

Schaber, G.G., McCauley, J.F., & Breed, C.S. (1997). The use of multifrequency and polarimetric SIR-C/X-SAR data in geologic studies of Bir Safsaf, Egypt. Remote Sensing of Environment, 59(2), 337-363, http://dx.doi.org/10.1016/S0034-4257(96)00143-5.

Szczechura, J., & Abd-Elshafy, E. (1988). Ostracodes and foraminifera from the Middle Miocene of the western coast of the Gulf of Suez, Egypt. Acta Palaeontologica Polonica, 33(4), 273–342.

Tawadros, E. (2001). Geology of Egypt and Libya. Taylor & Francis Group.

Toutin, T., & Gray, L. (2000). State-of-the-art of elevation extraction from satellite SAR data. ISPRS Journal of Photogrammetry and Remote Sensing , 55(1), 13-33, http://dx.doi.org/10.1016/S0924-2716(99)00039-8.

Ubukawa, T. (2013). An evaluation of the horizontal positional accuracy of Google and Bing satellite imagery and three roads data sets based on high resolution satellite imagery. New York: Center for International Earth Science Information Network (CIESIN), Earth Institute Columbia University, 16 pp..

Weather Underground Inc. (2014). Available online at http://www.wunderground.com (last accessed July 2014)

Youssef, A.M. (2009). Mapping the mega paleodrainage basin using shuttle radar topography mission in Eastern Sahara and its impact on the new development projects in Southern Egypt. Geospatial Information Science, 12(3), 182-190, http://dx.doi.org/10.1007/s11806-009-0057-8.

Zebker, H.A., & Villasenor, J. (1992). Decorrelation in interferometric radar echoes. IEEE Transactions on Geoscience and Remote Sensing, 30(5), 950-959, http://dx.doi.org/10.1109/36.175330.

FIGURE CAPTIONS

Fig. 1 – Location map; red box outlines the study area.

Fig. 2 – Subset of the Geological Map of Egypt; 1:500,000 scale, Sheet Siwa NH 35 SW (digitized from Klitzsch et al., 1987).

Fig. 3 – Examples of *garats* in the surroundings of Siwa (little mesas in A and B, buttes in C and D). Inset map shows the location of these geomorphologic landscapes.

Fig. 4 - Sketch map showing the possible course of the palaeo-Nile river during the Miocene (modified from Carmignani et al., 2009); the violet box indicates the location of the study area.

Fig. 5 – Location of the available CSKM scenes.

Fig. 6 – Examples of footprint and quick look of CSKM descending scenes for areas Nile1 (top) and Nile2 (bottom).

Fig. 7 - InSAR processing workflow.

Fig. 8 –InSAR DEMs; the Nile1 and Nile2 areas in both ascending and descending orbit configurations.

Fig. 9 - Radargrammetry workflow.

Fig. 10 – Radargrammetry DEMs; the Nile1 and Nile2 areas in both ascending and descending orbit configurations.

Fig. 11 – Example of differences in elevation between the SRTM DEM and the DEMs of the Nile2 area, calculated from granules in descending orbit using interferometry (left) and radargrammetry (right).

Fig.12 - 1Final DEM of the study area.

Fig. 13 – Drainage network extracted from the final DEM.

Fig.14 – Area characterized by the northwest-southeast trending drainage system (Quickbird scene from Google Earth™ in background); inset map shows a detailed view of the *garats* area.

Fig. 15 – Hypothesized pattern of the drainage network before the Late Messinian drawdown of the Mediterranean Sea.

Fig. 16 – Hypothesized pattern of the drainage network during the Late Messinian.

Fig. 17 – Hypothesized pattern of the drainage network during the Pliocene.

Fig. 18 – Hypothesized pattern of the drainage network during the Quaternary.

TABLES

Tab.1 – Statistics of elevation differences between the produced DEMs and the SRTM.

NILE 1		Mean (m)	Std. Dev. (m)	RMSE (m)
INSAR	Ascending	37	160	132
RADARGRAMMETRY	Ascending	3	13	12
INSAR	Descending	-19	19	22
RADARGRAMMETRY	Descending	-3	19	17
NILE 2		**Mean (m)**	**Std. Dev. (m)**	**RMSE (m)**
INSAR	Ascending	3.9	10	9
RADARGRAMMETRY	Ascending	1	8	8
INSAR	Descending	-7	12	12
RADARGRAMMETRY	Descending	-6	9	10

Tab.2 - Classification of elevation residuals and relative percentages.

Range of residuals (m)	Nile1 Ascending Interferom.	Nile1 Ascending Radargramm.	Nile1 Descending Interferom.	Nile1 Descending Radargramm.	Nile2 Ascending Interferom.	Nile2 Ascending Radargramm.	Nile2 Descending Interferom.	Nile2 Descending Radargramm.
Min - -40	36.3%	0.1%	16.7%	0.8%	0.0%	0.0%	1.7%	0.7%
-40 - -30	2.5%	0.4%	18.5%	2.1%	0.2%	0.1%	3.4%	1.5%
-30 - -20	2.5%	1.6%	15.8%	12.2%	1.2%	1.3%	10.8%	4.8%
-20 - -10	2.2%	11.9%	15.2%	32.2%	6.7%	7.2%	24.1%	21.4%
-10 - 0	2.1%	29.4%	14.3%	23.6%	28.7%	35.1%	32.4%	58.8%
0 - 10	2.0%	29.5%	12.7%	12.8%	39.1%	44.1%	20.3%	9.3%
10 - 20	2.1%	16.2%	5.4%	5.6%	19.4%	10.1%	6.6%	2.0%

20 - 30	2.1%	6.5%	1.0%	3.4%	3.3%	1.7%	0.7%	0.9%
30 - 40	2.1%	2.7%	0.3%	2.4%	0.9%	0.3%	0.1%	0.3%
40 - Max	46.1%	1.7%	0.1%	4.9%	0.5%	0.1%	0.1%	0.2%
	100.0%	100.0%	100.0%	100.0%	100.0%	100.0%	100.0%	100.0%

Tab.3 – Statistics of elevation differences among the produced DEMs of the Nile2 area (ascending orbit - descending orbit).

NILE2		**Mean (m)**	**Std. Dev. (m)**	**RMSE (m)**
INSAR ASCENDING	INSAR DESCENDING	-14	12	13
RADARGRAMMETRY ASCENDING	RADARGRAMMETRY DESCENDING	-7	10	10
RADARGRAMMETRY ASCENDING	INSAR DESCENDING	-14	12	15
INSAR ASCENDING	RADARGRAMMETRY DESCENDING	-12	12	12

Figure 1
Click here to download high resolution image

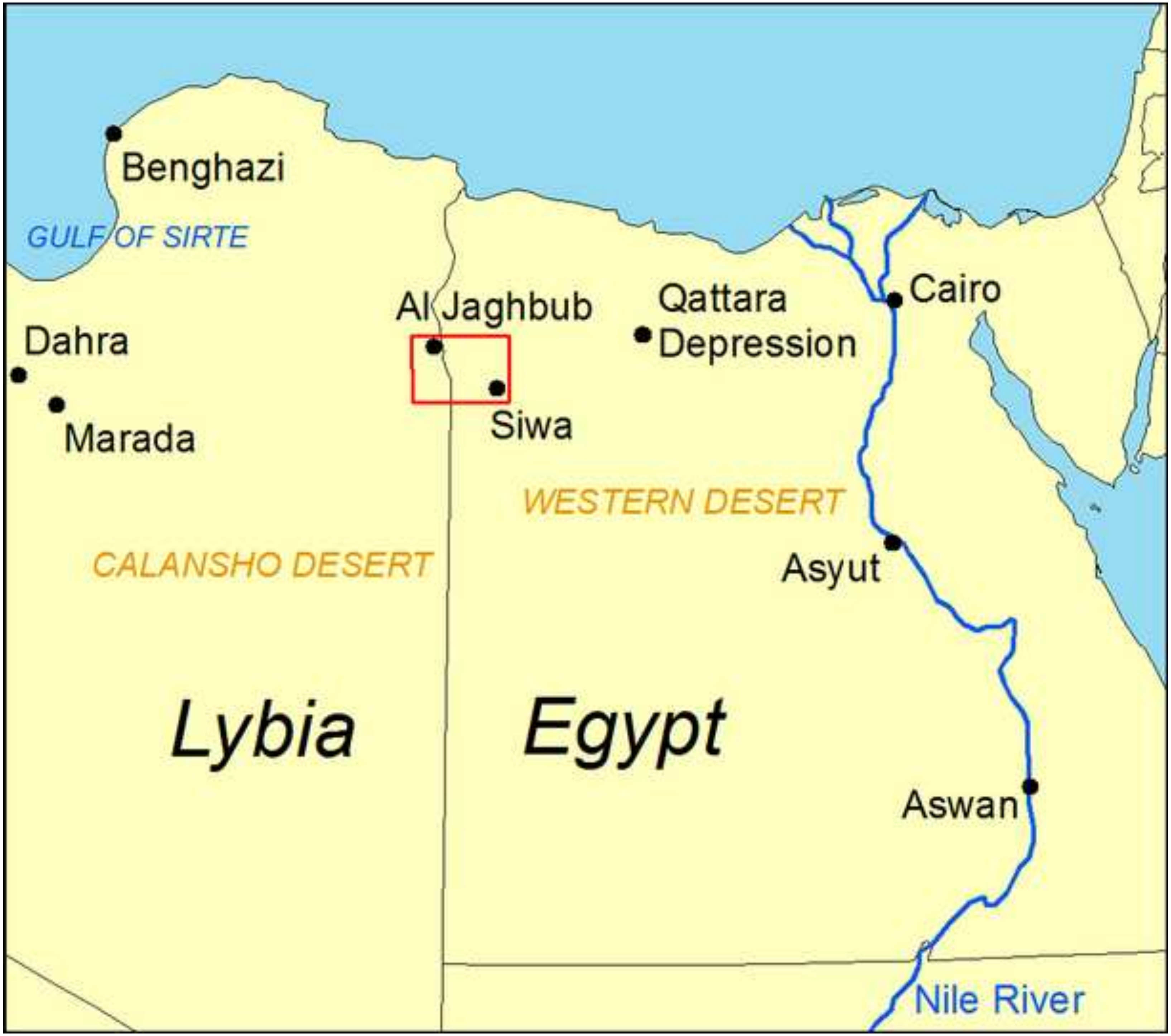

Figure 2
Click here to download high resolution image

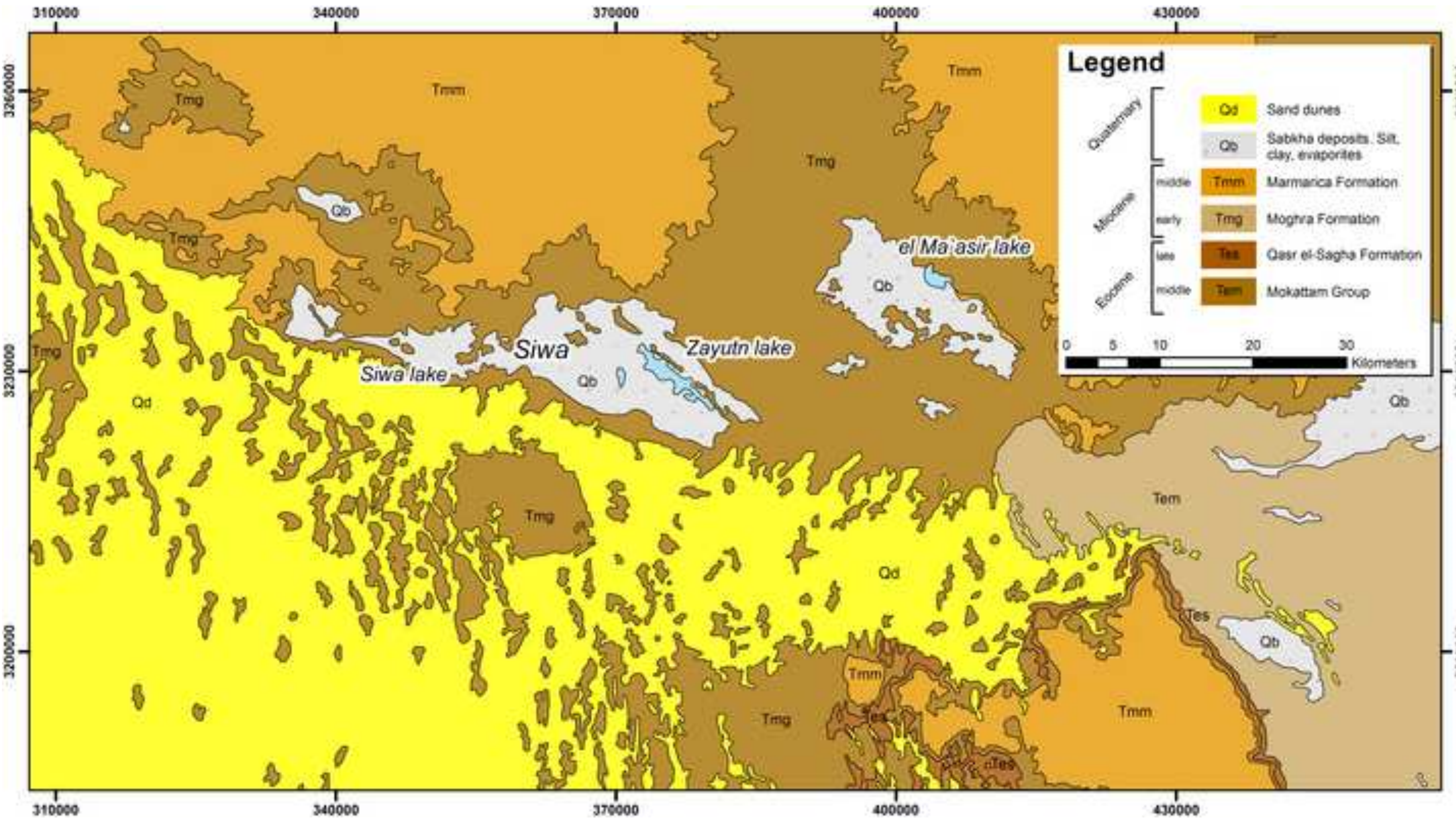

Figure 3

Click here to download high resolution image

Figure 4
Click here to download high resolution image

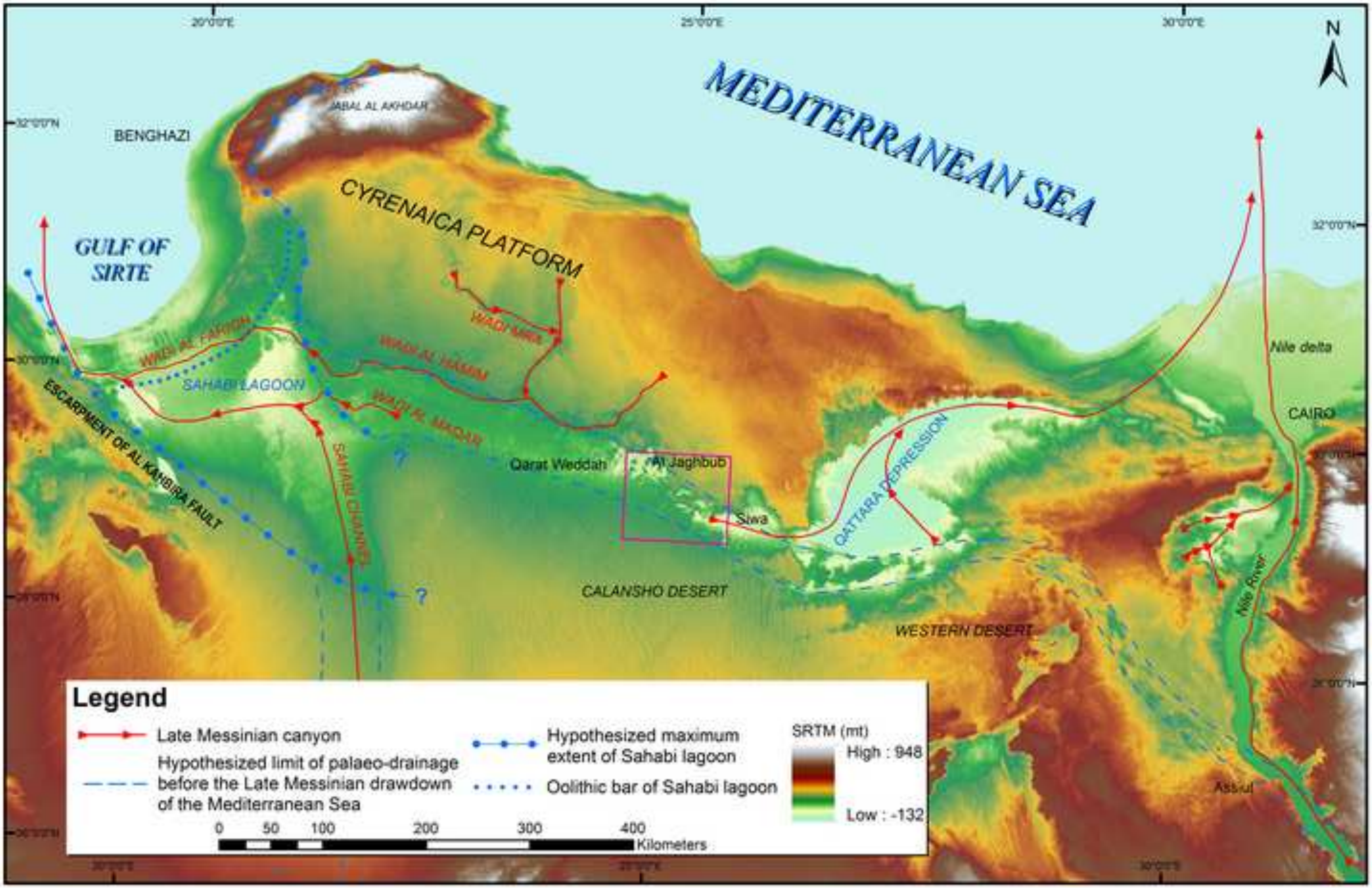

Figure 5
Click here to download high resolution image

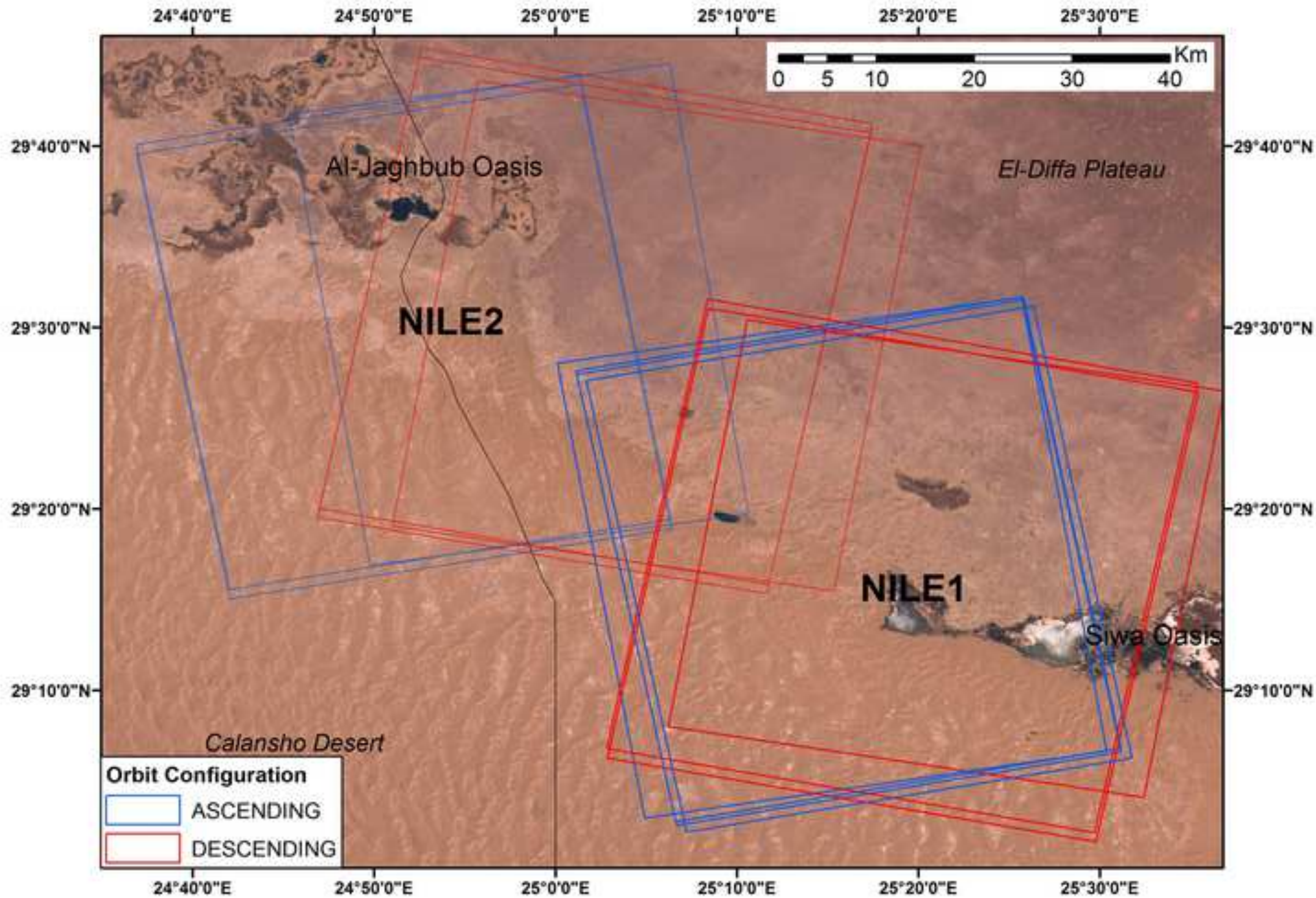

Figure 6

Click here to download high resolution image

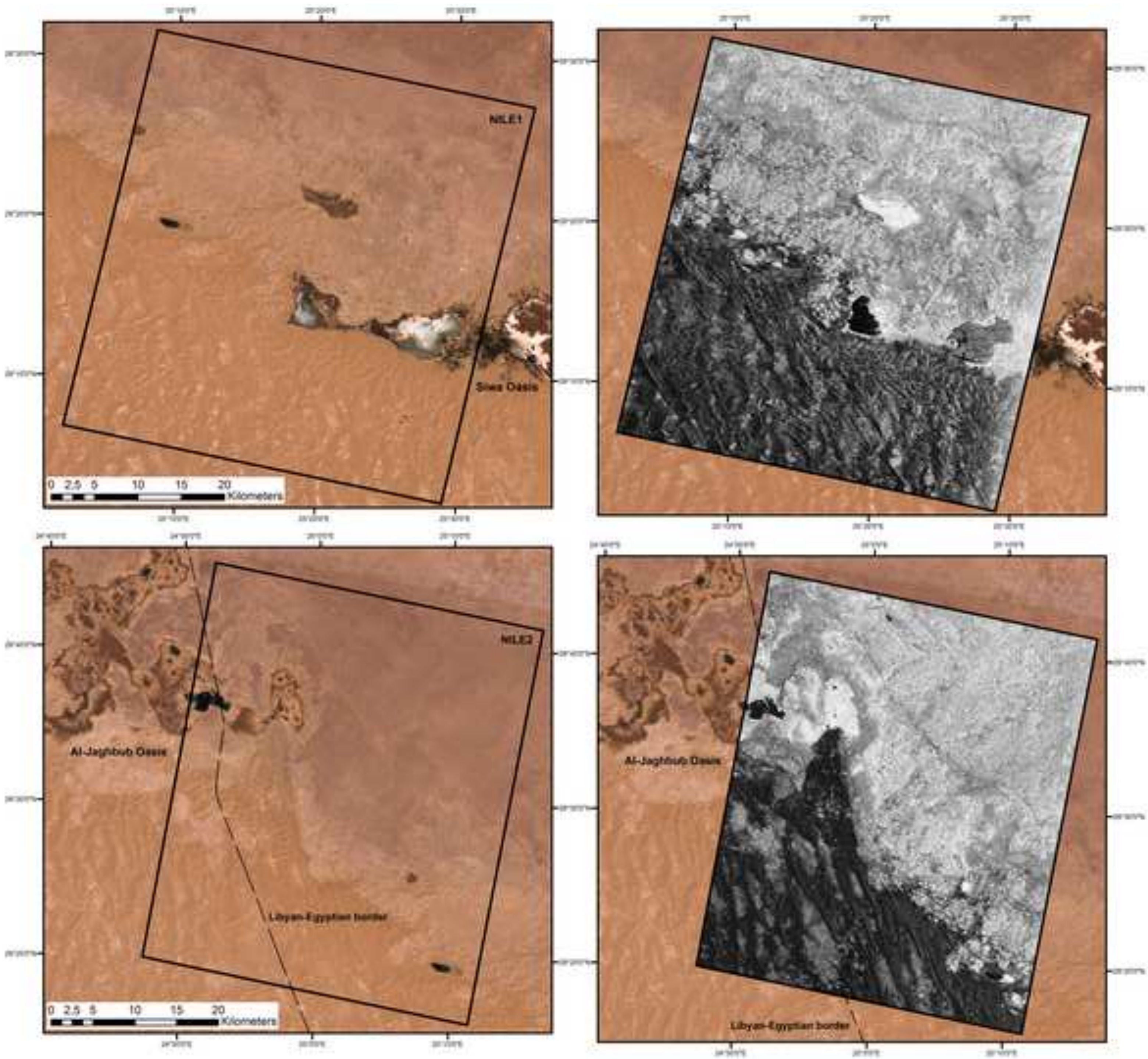

Figure 7

Click here to download high resolution image

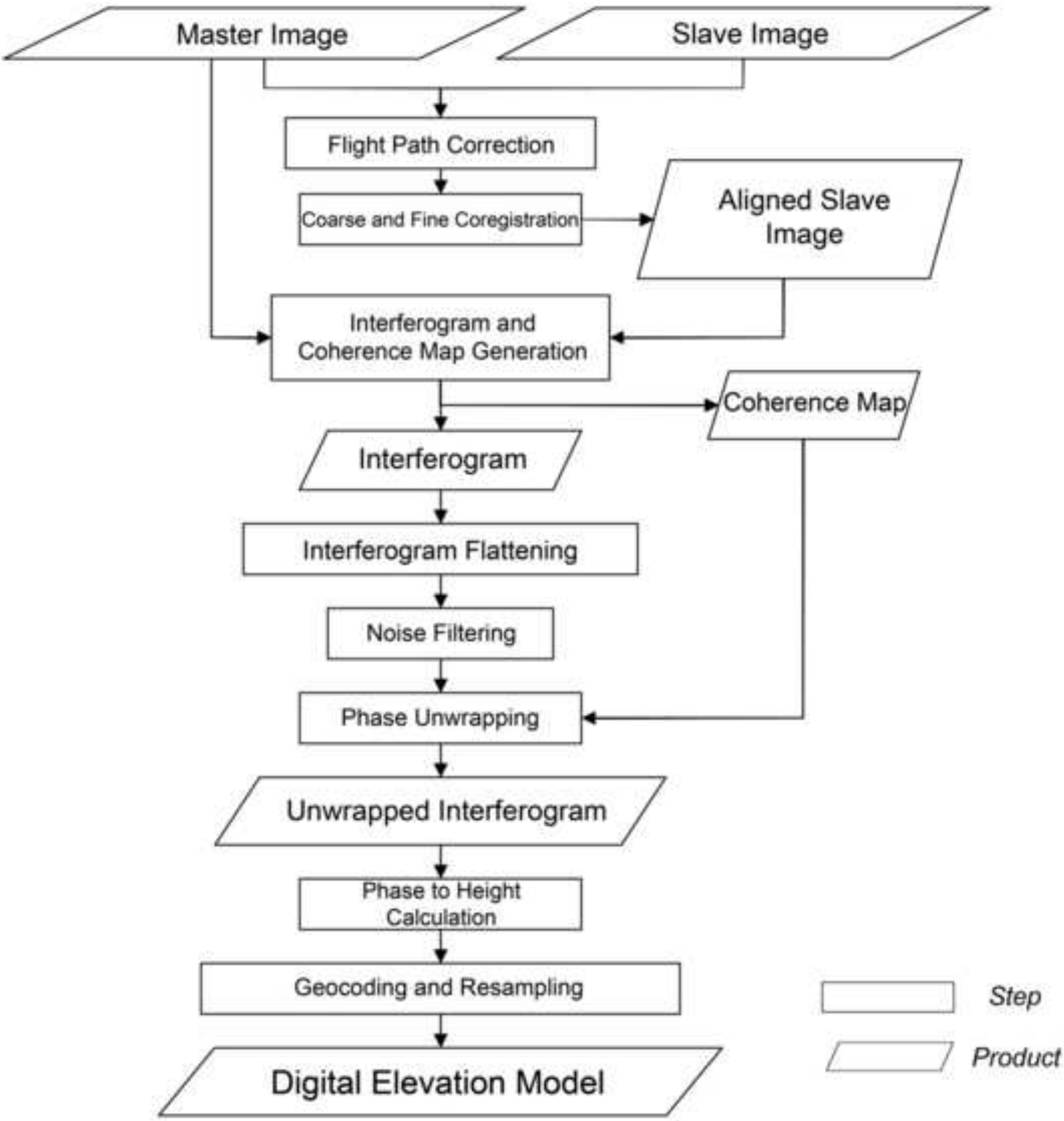

Figure 8
Click here to download high resolution image

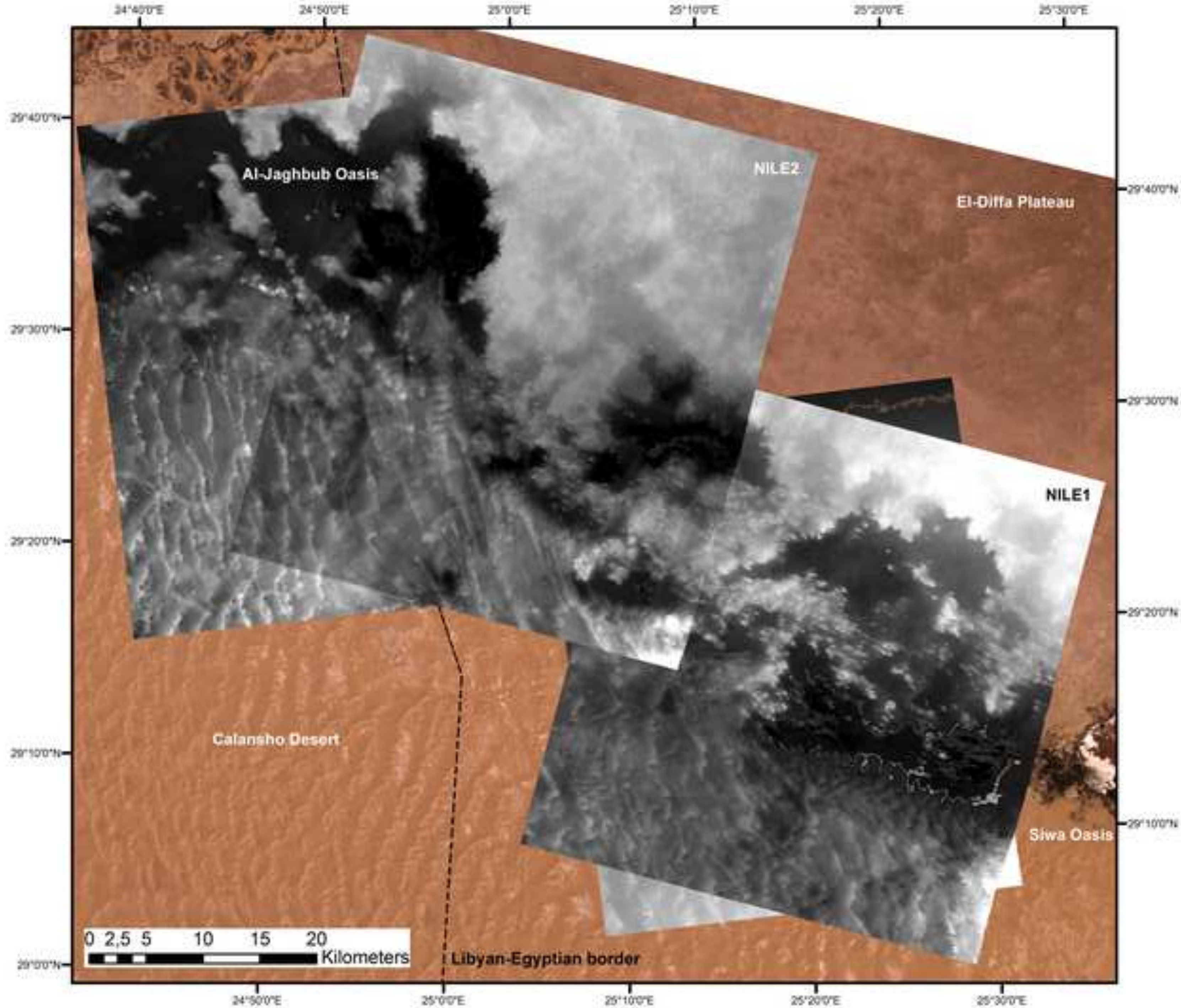

Figure 9
Click here to download high resolution image

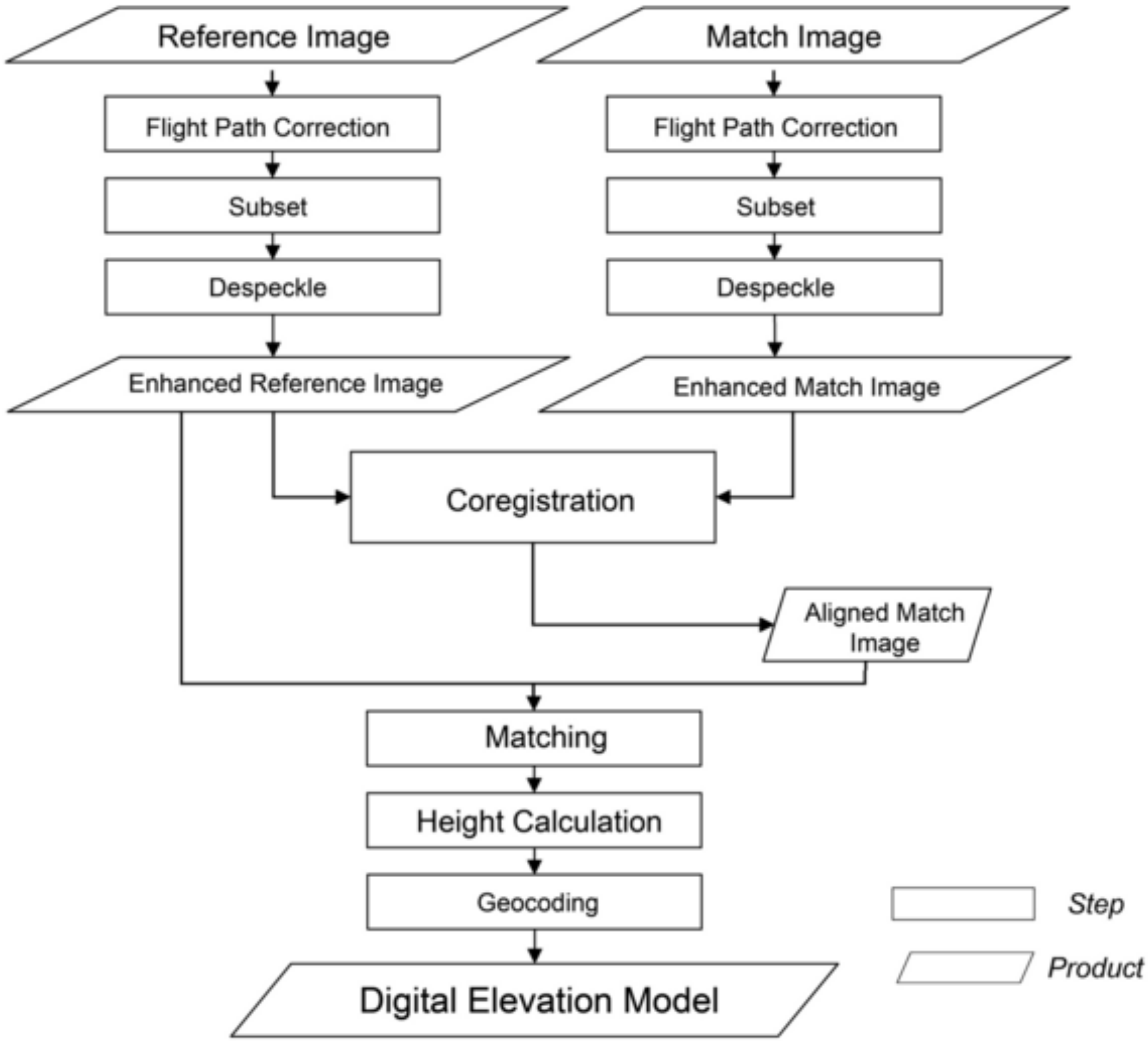

Figure 10

Click here to download high resolution image

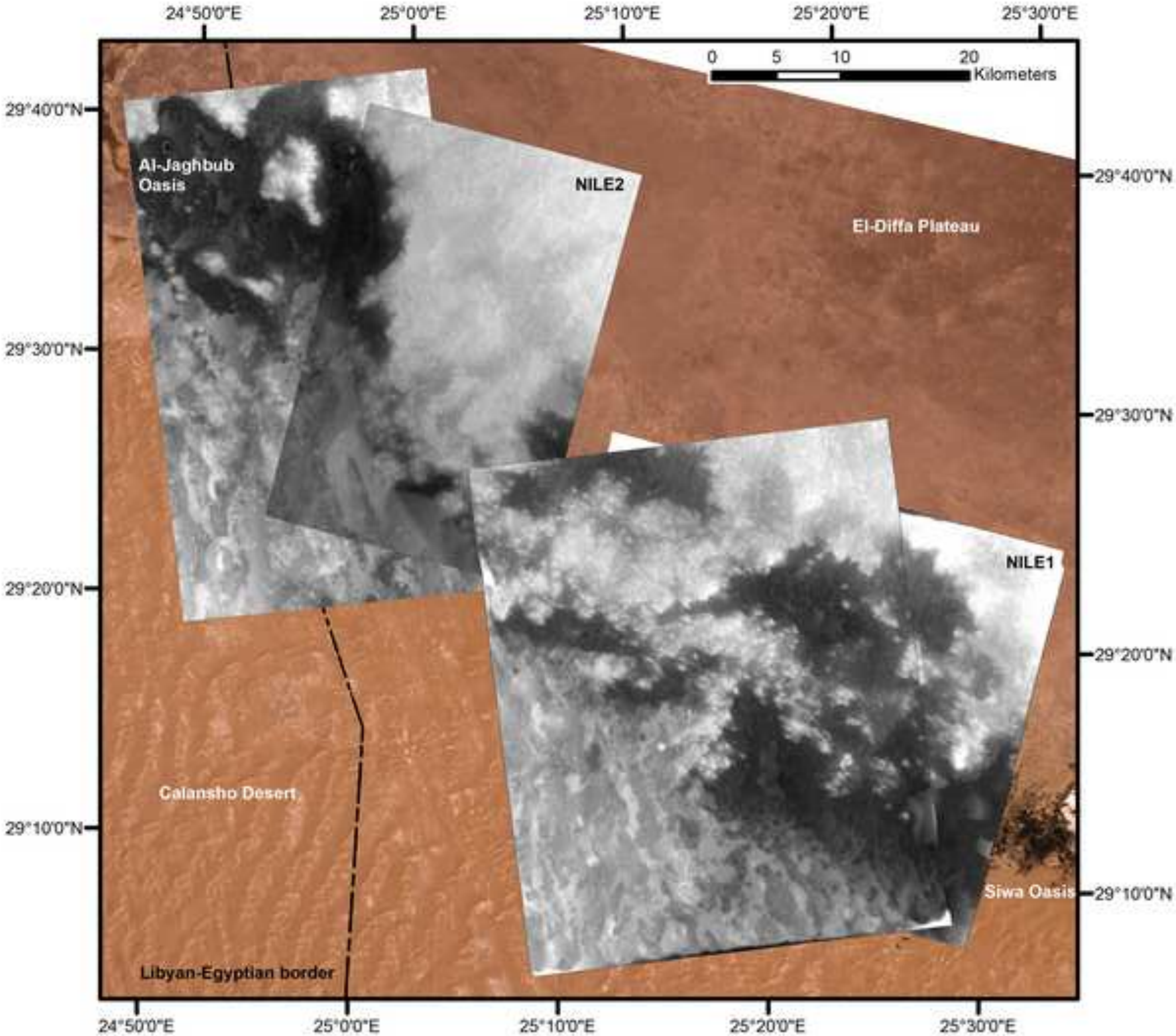

Figure 11
Click here to download high resolution image

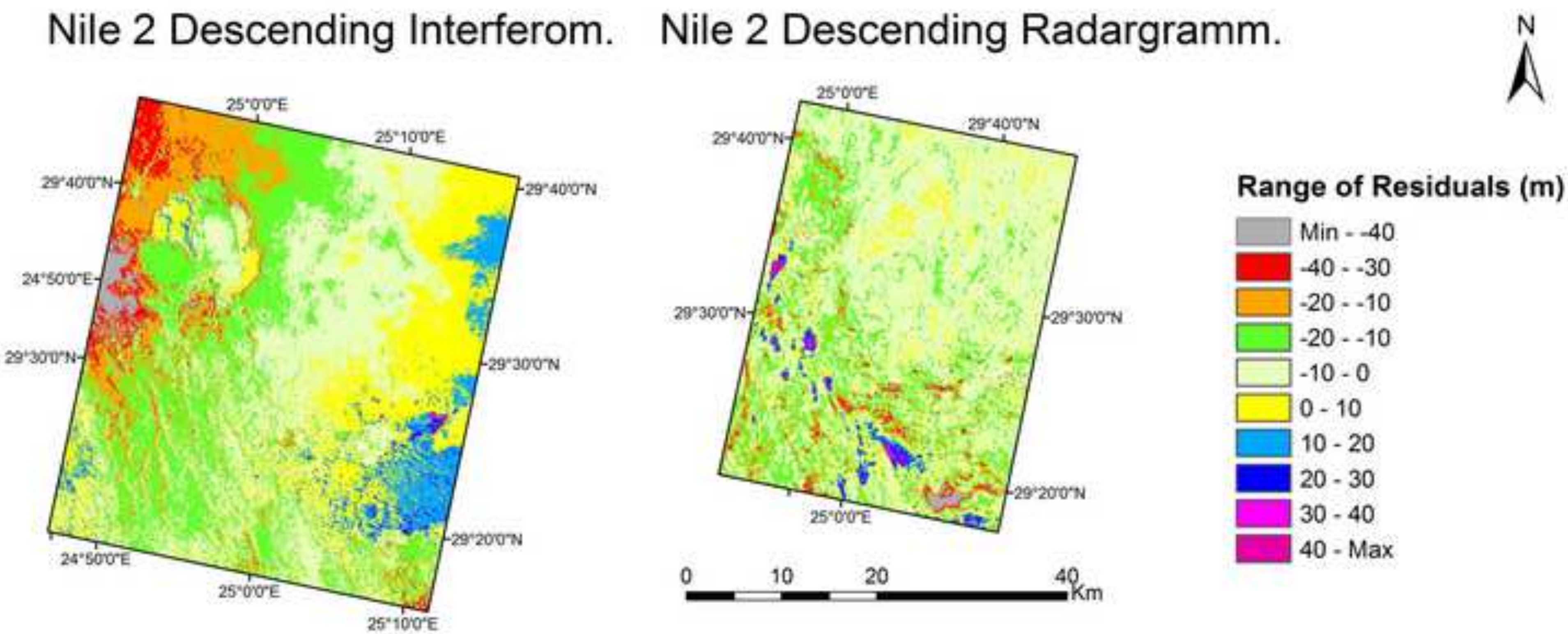

Figure 12
Click here to download high resolution image

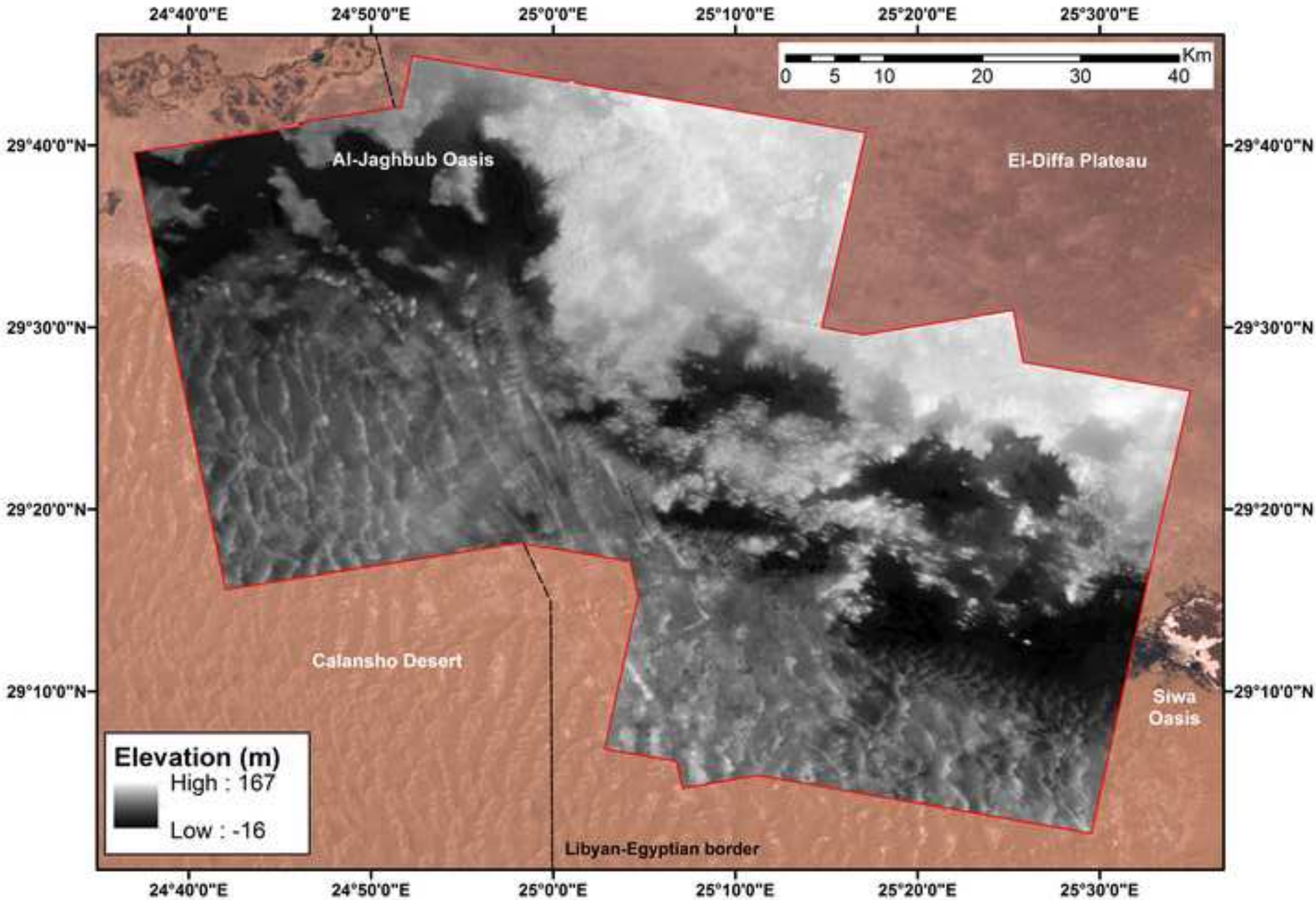

Figure 13
Click here to download high resolution image

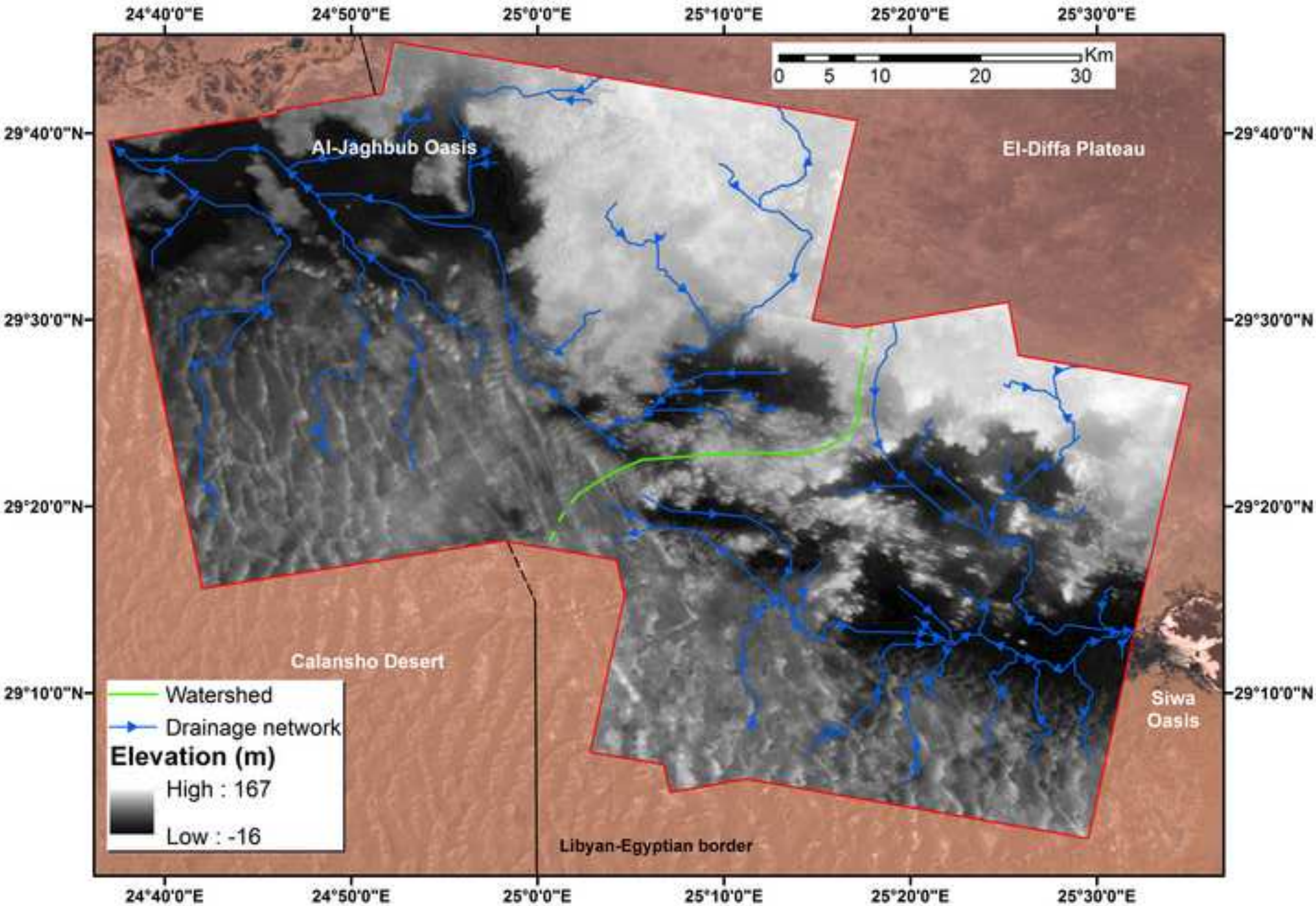

Figure 14
Click here to download high resolution image

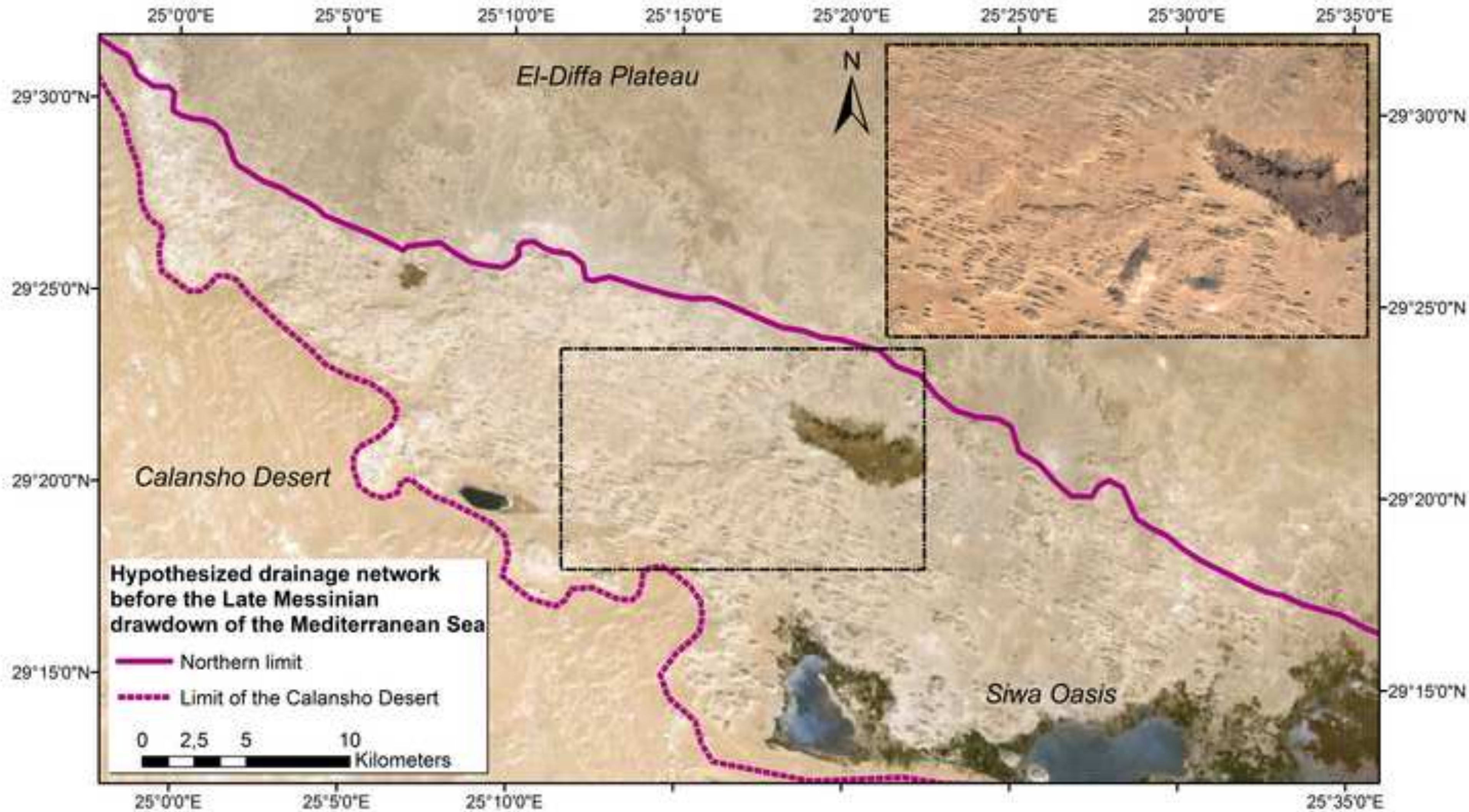

Figure 15
Click here to download high resolution image

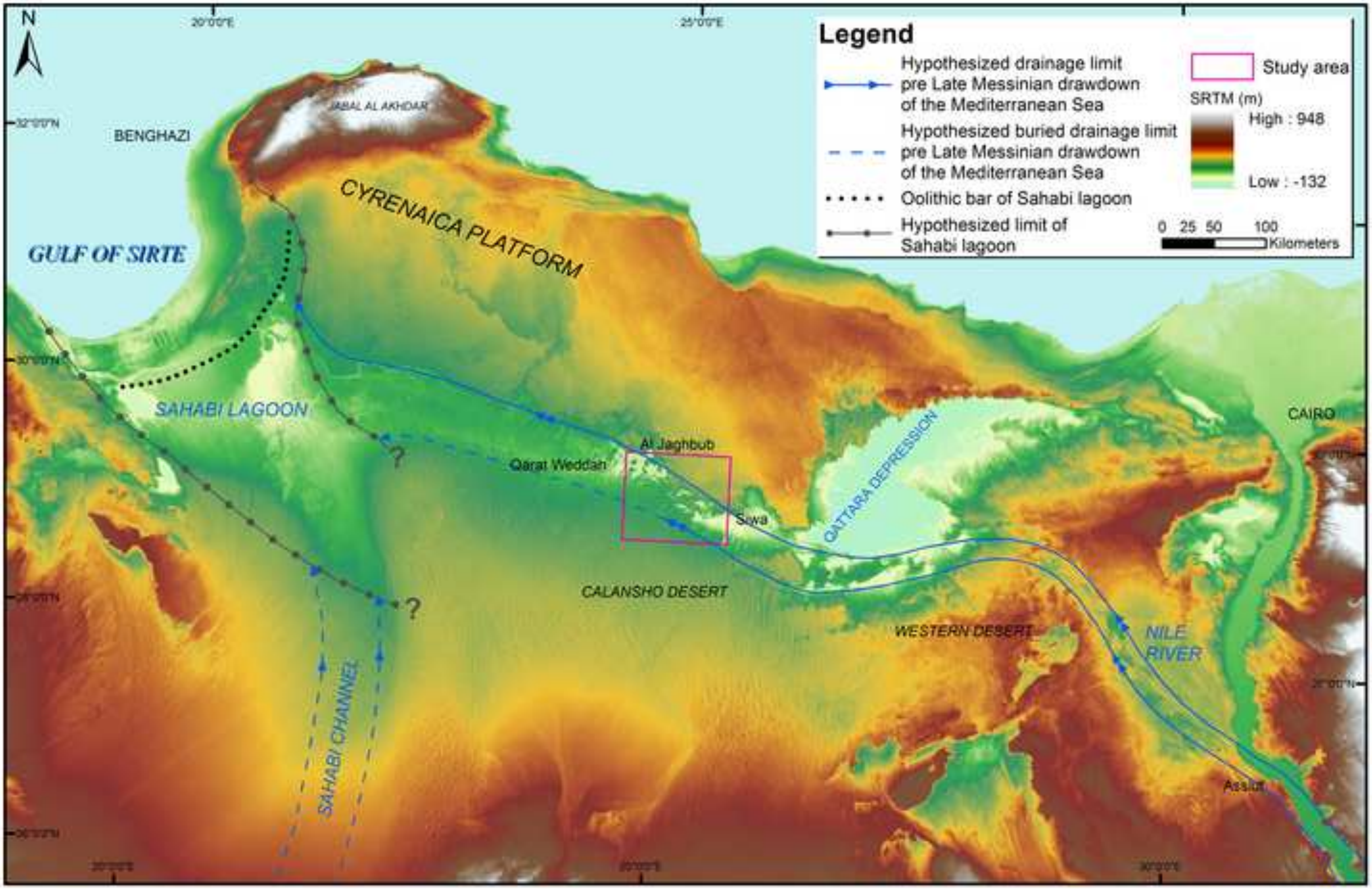

Figure 16
Click here to download high resolution image

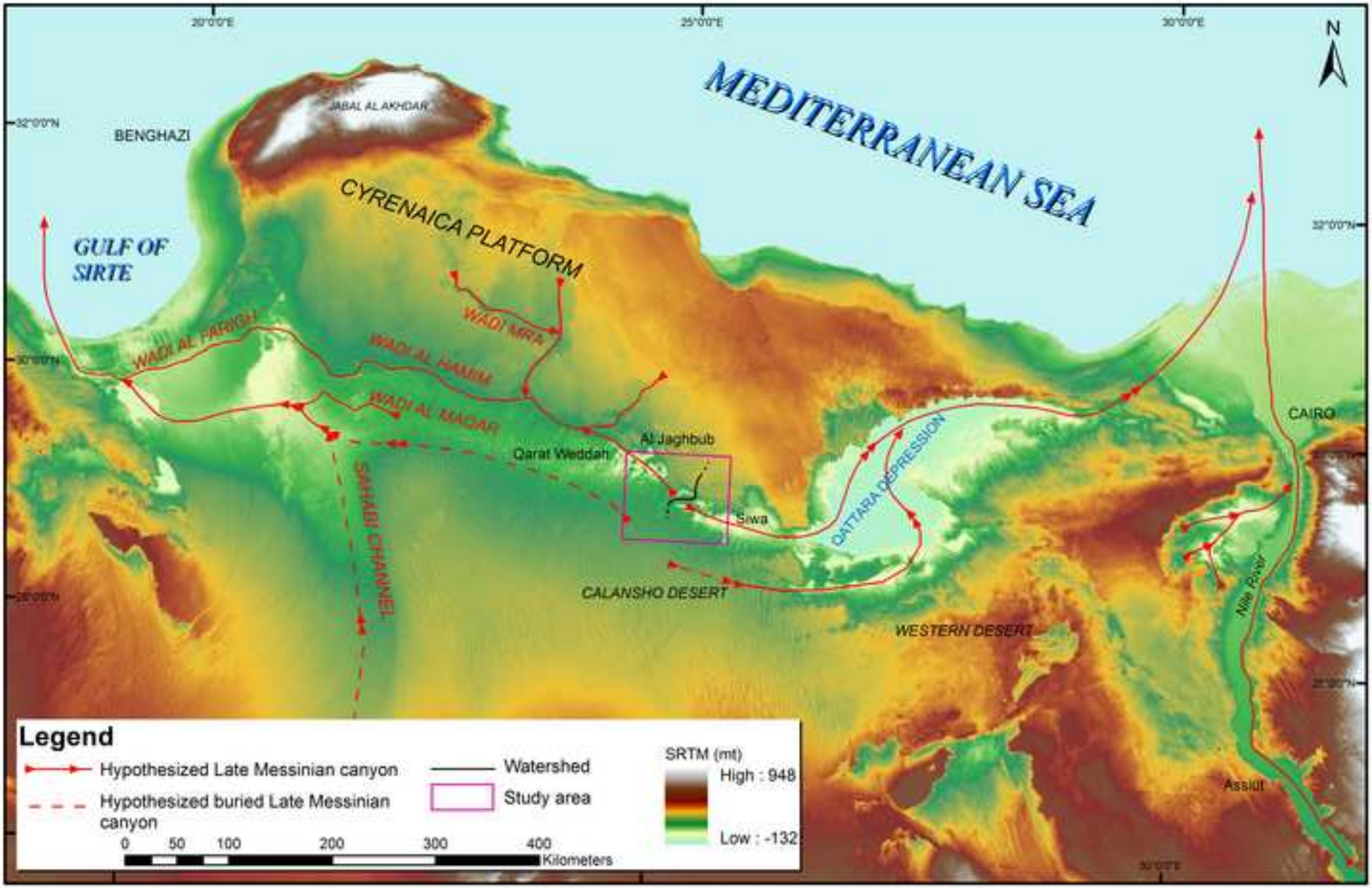

Figure 17
Click here to download high resolution image

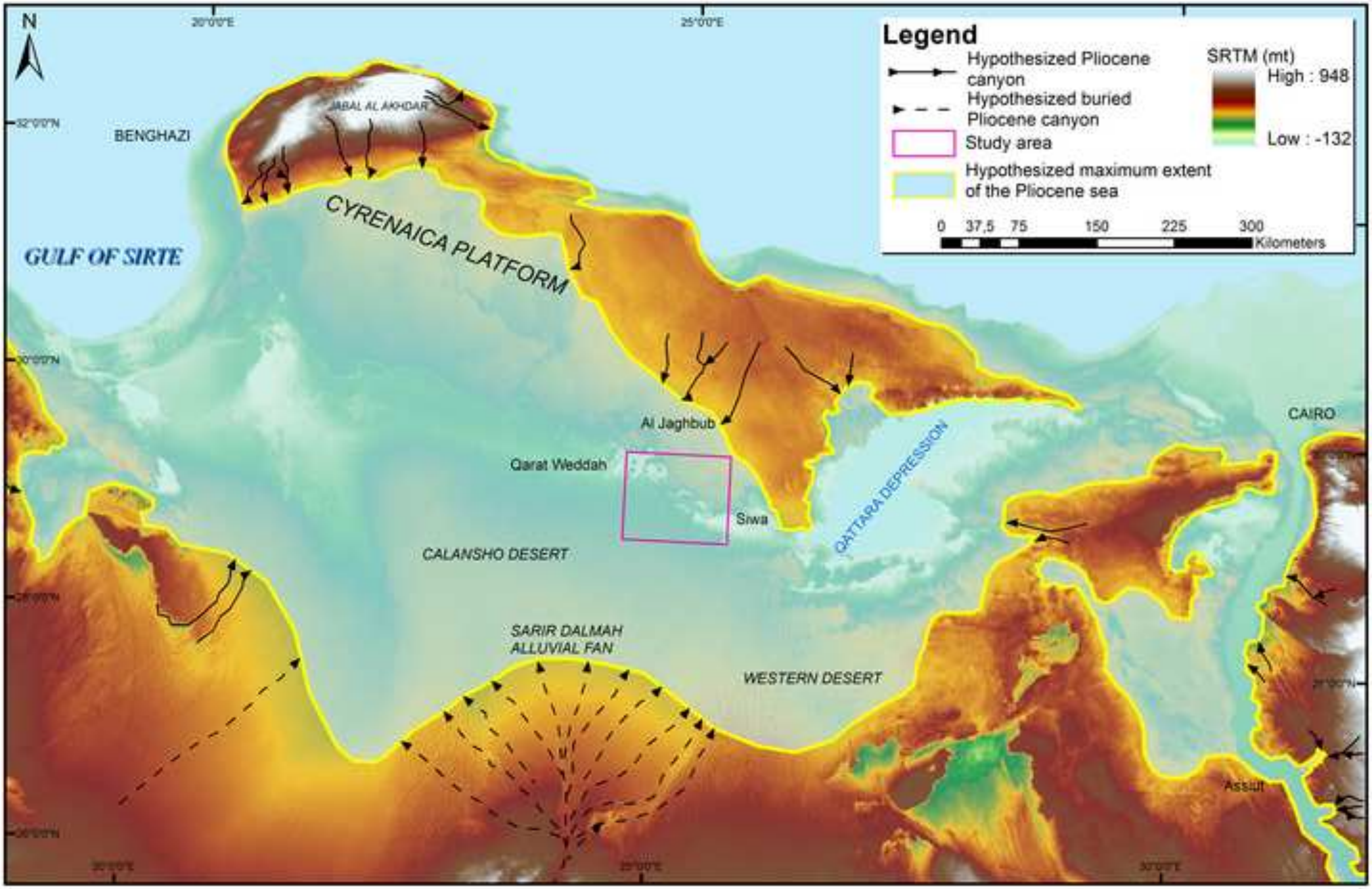

Figure 18
Click here to download high resolution image